Science of the Total Environment 755 (2021) 142712

Contents lists available at ScienceDirect

Science of the Total Environment

journal homepage: www.elsevier.com/locate/scitotenv

Simulated aging processes of black carbon and its impact during a severe winter haze event in the Beijing-Tianjin-Hebei region

Donglin Chen [a], Hong Liao [a,*], Yang Yang [a,*], Lei Chen [a], Hailong Wang [b]

[a] Jiangsu Key Laboratory of Atmospheric Environment Monitoring and Pollution Control, Jiangsu Engineering Technology Research Center of Environmental Cleaning Materials, Collaborative Innovation Center of Atmospheric Environment and Equipment Technology, School of Environmental Science and Engineering, Nanjing University of Information Science & Technology, Nanjing, Jiangsu, China

[b] Atmospheric Science and Global Change Division, Pacific Northwest National Laboratory, Richland, WA, USA

HIGHLIGHTS

- The aging processes decreased near-surface BC concentration by 0.7 μg m^{-3} in BTH.
- The aging processes increased the BC particle size in BTH.
- The aging processes of BC further inhibited the development of PBL.
- The aging processes of BC increased near-surface $PM_{2.5}$ concentration in BTH.
- The aging processes of BC decreased near-surface O_3 concentration by 2.2 ppbv in BTH.

GRAPHICAL ABSTRACT

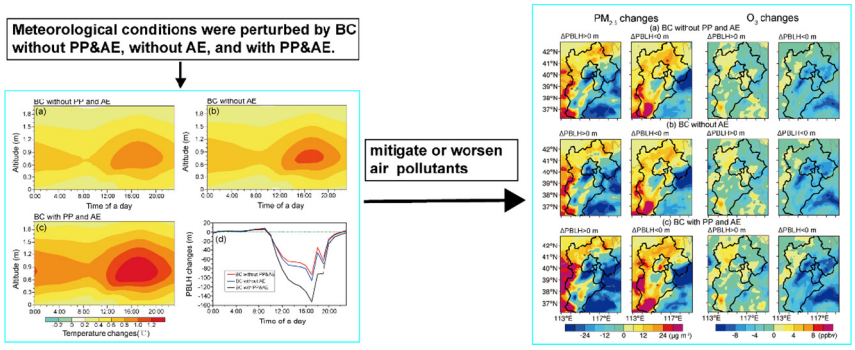

ARTICLE INFO

Article history:
Received 6 August 2020
Received in revised form 18 September 2020
Accepted 27 September 2020
Available online 2 October 2020

Editor: Pingqing Fu

Keywords:
Black carbon
Physical aging processes
Absorption enhancement
Direct radiative effects
Severe haze pollution in BTH

ABSTRACT

Black carbon (BC) can mitigate or worsen air pollution by perturbing meteorological conditions. BC aging processes strongly influence the evolution of the particle size, concentration, and optical properties of BC, which determine its influence on meteorology. Here, we use the online coupled Weather Research and Forecasting-Chemistry (WRF-Chem) model to quantify the role of BC aging processes, including physical processes (PP) and absorption enhancement (AE), in causing BC-induced meteorological changes and their associated feedbacks to $PM_{2.5}$ (particulate matter less than 2.5 μm in diameter) and O_3 concentrations during a severe haze event in the Beijing-Tianjin-Hebei (BTH) region during 21–27 February 2014. Our results show that, compared to those from the simulation without PP, the simulated near-surface BC concentration and BC mass loading in the BTH region decreased by 6.6% and 12.1%, respectively, when PP were included. PP increased the proportion of large BC (particle diameter greater than 0.312 μm) below 1000 m from 28 to 33% to 59–64% in the BTH region. When both PP and AE were included in the simulation, the reduction in PBL height due to the BC-PBL interaction was 116.3 m (20.7%), compared to reductions of 75.7 m (13.5%) without AE and 66.6 m (11.9%) without PP and AE. However, during this haze event, anomalous northeasterly winds were produced by the direct radiative effect of BC, which further affected aerosol mixing and transport. Due to their combined impacts on multiple meteorological factors, the direct radiative effects of BC without PP and AE, without AE, and with PP and AE increased the surface concentrations of $PM_{2.5}$ by 8.3 μg m^{-3} (by 6.1% relative to the mean value), 6.1 μg m^{-3} (4.5%) and 9.6 μg m^{-3} (7.0%), respectively, but decreased the surface O_3 concentrations by 2.8 ppbv (7.4%), 4.0 ppbv (9.0%) and 5.0 ppbv (10.8%) on average in the BTH region during 21–27 February 2014.

* Corresponding authors.
E-mail addresses: hongliao@nuist.edu.cn (H. Liao), yang.yang@nuist.edu.cn (Y. Yang).

https://doi.org/10.1016/j.scitotenv.2020.142712
0048-9697/

1. Introduction

Black carbon (BC), an important component of atmospheric aerosols, is emitted mainly from the incomplete combustion of fossil fuels, biofuels, or biomass. BC particles can strongly absorb solar radiation in the atmosphere, which changes the Earth's radiation balance (Bond et al., 2013; Yang et al., 2017, 2019). They can also affect atmospheric visibility and human health (Ji et al., 2017). BC has been found to play an important role in aerosol-meteorology interactions during haze events. Ding et al. (2016) examined the interactions between BC and the planetary boundary layer (PBL) during heavy haze days (i.e., days with a maximum $PM_{2.5}$ concentration over 200 μg m^{-3}) in megacities in China in December 2013 using the Weather Research and Forecasting model coupled with Chemistry (WRF-Chem). They found that the air temperature at 300–1200 m was increased by 1–1.5 °C at approximately 4:00 pm local time due to the presence of BC, which favoured the formation of an inversion layer and caused a drop in PBL height by approximately 160 m (36%). In addition to its impact on the PBL, researchers have also found that BC changes the land-sea thermal contrast and induces circulation anomalies during periods of heavy pollution (Gao et al., 2016; Qiu et al., 2017; Lou et al., 2019; Q. Ding et al., 2019). Q. Ding et al. (2019) showed that the direct radiative forcing of BC could cause a cooling effect on surface air temperature over land and warming over sea due to the sea surface being more capable of storing heat than the land and hence enhance advection between land and sea in the Yangtze River Delta region during a haze event in December 2013.

BC can affect the concentration of atmospheric pollutants by changing meteorological conditions (e.g., temperature, PBL height and wind), especially during heavy pollution events (Forkel et al., 2011; Gao et al., 2018; Huang et al., 2018). Gao et al. (2016) reported that $PM_{2.5}$ concentrations increased by approximately 14.4 μg m^{-3} in Shijiazhuang but decreased in the areas south of Beijing due to radiative feedback from BC in WRF-Chem. Qiu et al. (2017) found that in their WRF-Chem simulation, BC shortwave radiative forcing at the surface was −18.0 W m^{-2}, and the concentration of $PM_{2.5}$ increased by 2.1 μg m^{-3} (1.0%) on average over the North China Plain (NCP) due to the direct radiative effect of BC in a haze event during 21–27 February 2014. Additionally, using WRF-Chem, Gao et al. (2018) found that the surface-layer ozone decreased by up to 16.4 ppb at 12:00 pm in Nanjing due to the direct radiative effect of BC, which inhibited the development of PBL and thus reduced O_3 transport from high altitudes to the surface.

Upon emission, fresh BC particles are small. They then start to grow through coagulation, condensation and mixing processes (Moteki et al., 2007; Laborde et al., 2013; Watson-Parris et al., 2019). These processes are referred to as the aging of BC. Previous observational studies in China have reported that BC aging has a large influence on its particle size and optical properties, which further enhances the impact of BC on meteorological conditions (Peng et al., 2016; Wu et al., 2016; Q. Ding et al., 2019). Laboratory experiments and theoretical computation have shown that a thick coating of weakly absorbing species can significantly enhance the absorption efficiency of BC above that of uncoated BC through refraction and internal reflections (Fuller et al., 1999; Schnaiter et al., 2005; Bond et al., 2016). The coating acts as a lens that amplifies the absorption of BC, which is called the "lensing effect". The BC light absorption enhancements depend on the size and mixing state of the BC-containing particles and the thickness of the coating (Q. Wang et al., 2014; Wu et al., 2016; Liu et al., 2017). Wu et al. (2016) measured the light absorption coefficients of BC with a ground-based single-particle soot photometer (SP2) and showed that the average values of light absorption coefficients were 8.2 ± 5.2 Mm^{-1} in non-hazy periods and 33.1 ± 20.2 Mm^{-1} in hazy periods in urban Beijing during the extremely polluted winter of 2013; these values were explained by the increase in the thickly coated number fraction of BC. Based on data from a novel quasi-atmospheric aerosol evolution study (QUALITY) chamber, Peng et al. (2016) noted that after BC particles had been in the atmosphere in Beijing for 2.3 h, they were completely aged, and the light absorption of the BC particles was enhanced by 2.4 times. Other previous studies also reported that BC light absorption was increased by a factor of 1.1–3.2 due to the aging processes (Jacobson, 2001; Cappa et al., 2012; Xie et al., 2019). S. Ding et al. (2019) observed that the BC core mass median diameter (MMD) increased with increasing BC mass concentration in both continental Europe and Beijing to MMD = 0.15–0.21 μm when the BC concentration was less than 0.4 μg m^{-3} and MMD = 0.16–0.23 μm when the BC concentration was over 1 μg m^{-3}. They concluded that coagulation processes played an important role under conditions of high BC mass loadings.

BC aging has also been extensively investigated in modelling studies (Liu et al., 2016; Matsui, 2016a; Matsui, 2016b; Chen et al., 2017; Matsui et al., 2018; Zhang et al., 2019). The aging timescale in the models is defined as the time required for BC particles to transform from their freshly emitted hydrophobic state to a hydrophilic state, which has been reported to be 0.19–3.1 days (Lohmann et al., 1999; Liu et al., 2008). Chen et al. (2017) calculated the BC aging time by tracking the mass concentrations of soluble species that formed coatings on BC; using the Nested Air Quality Prediction Modelling System with Advanced Particle Microphysics (NAQPMS+APM), they showed that the aging time of BC was shorter than 2 h during the day and more than 2 days at night in a polluted atmosphere because the hydrophilic fraction of the BC coating was much larger during the day than at night. Zhang et al. (2019) used an aging-resolved model with externally mixed aerosols to track the aging time of elemental carbon (EC) emitted in southeastern Texas during 24–31 August 2000 and calculated the optical properties of EC at different aging stages and sizes. They found that there was a 35% difference in the extinction coefficient of aerosols caused by their new EC aging-resolved treatment. Matsui et al. (2018) used an aerosol bin module to simulate BC aging with the Community Atmosphere Model version 5 (CAM5), which considers condensation and coagulation processes for BC aging, to quantify the range of the direct radiative effects of present-day BC that are related to the aging processes. They reported that the global BC direct radiative effect was amplified by 5–7 times (0.18–0.42 W m^{-2}) with a multiple BC mixing state compared to that obtained with a single BC mixing state within the same model framework.

As mentioned above, although many previous studies have confirmed the impact of BC on pollutants and tracked the aging time of BC under various meteorological and pollution conditions, the direct radiative effects of BC with and without aging processes on meteorological parameters and atmospheric pollutants have rarely been discussed in the existing literature. Considering the high relative humidity, low wind speed and relatively high emissions in China, which are conducive to the rapid accumulation and aging processes of BC particles (Zhang et al., 2015; Peng et al., 2016; Wu et al., 2016), it is important to examine the role of BC aging during heavy pollution events under these conditions.

Beijing, the capital city of China, has reported many severe haze events in recent decades (Gao et al., 2015; Wang et al., 2015; Ji et al., 2018). Previous studies have reported that $PM_{2.5}$ and BC are relatively high in Beijing in February (Ji et al., 2017). In this study, we use the online regional chemistry-climate coupled model WRF-Chem to systematically examine the impact of BC with and without aging by physical processes (PP) and absorption enhancement (AE) on meteorological factors and pollutants in the Beijing-Tianjin-Hebei (BTH) region during a severe haze event during 21–27 February 2014. During this haze event, the observed average concentrations of $PM_{2.5}$ and BC in Beijing were as high as 224.8 μg m^{-3} and 9.7 μg m^{-3}, respectively. We pay special attention to (1) how the mass concentration and particle size of BC change due to physical BC aging processes in the BTH region during the haze event and (2) differences in the direct radiative effects of BC with and without PP/AE.

The descriptions of the WRF-Chem model, methods, observational data sets and numerical experiments are presented in Section 2. Section 3 evaluates the WRF-Chem simulated meteorological conditions and pollutants by comparing them with observational data. Section 4 describes the changes in BC concentrations and particle size due to different physical processes during the severe haze event, and Section 5

discusses aerosol-meteorology interactions in the BTH region. The conclusions of this study are given in Section 6.

2. Model and observations

2.1. Model configurations

The WRF-Chem model version 3.7.1 with aerosol-radiation interactions (Chapman et al., 2009) was used to simulate a severe winter haze event in BTH. The WRF-Chem model adopted the Lambert projection and two nested domains with grid resolutions of 30 km (d01) and 10 km (d02). The number of vertical layers was 29, and the barometric pressure was up to 50 hPa. The horizontal grids were 100 × 100 (d01) and 58 × 76 (d02). The outer domain (d01) covered most of China with a central longitude and latitude of 108°E and 34°N, respectively, and the inner domain (d02) covered the BTH region and northeast Shandong Province (Fig. S1). The parameterization schemes of the physical and chemical processes of the WRF-Chem model selected in this study are shown in Table S1. The initial and boundary conditions of the model meteorological fields are derived from global reanalysis data (1° × 1°) from NCEP (National Center for Environmental Prediction). Simulation results from MOZART-4 (Model for Ozone And Related chemical Tracers-4) provided the initial and lateral boundary conditions for chemical substances (Emmons et al., 2010). In the WRF-Chem model, BC and other aerosols are assumed to be internal mixture and are divided into 8 bins by particle size (i.e., 0.039–0.078 μm (bin 1), 0.078–0.156 μm (bin 2), 0.156–0.312 μm (bin 3), 0.312–0.625 μm (bin 4), 0.625–1.25 μm (bin 5), 1.25–2.5 μm (bin 6), 2.5–5.0 μm (bin 7) and 5.0–10 μm (bin 8)). The volume-mean mixing method is used in the model to calculate the bulk optical properties of aerosols (Stelson, 1990; Barnard et al., 2010).

2.2. Emission inventories

The anthropogenic emissions in 2014 were obtained from the Multiresolution Emission Inventory for China (MEIC) database (http://www.meicmodel.org/, last access: 22 April 2020). The aerosol and precursor emissions included sulfur dioxide (SO_2), nitrogen oxides (NO_X), carbon monoxide (CO), non-methane volatile organic compounds (NMVOC), ammonia (NH_3), BC, organic carbon (OC), $PM_{2.5}$, PM_{10} and carbon dioxide (CO_2), which were categorized into the agriculture, industry, residence, transport and power-generation sectors (Li et al., 2017). The biogenic emission sources, including isoprene, terpene and other substances emitted by plants, were obtained from MEGANv2.04 (Model of Emissions of Gases and Aerosols from Nature v2.04) (Guenther et al., 2006). Biomass burning emissions were obtained from the Fire Inventory from NCAR (FINN) datasets (Wiedinmyer et al., 2011).

2.3. Numerical experiments and methodology

To quantify the aging processes of BC and examine the direct radiative effects of BC associated with its aging through physical processes and absorption enhancement on meteorological conditions and atmospheric pollutants during a haze event in the BTH region, we conducted the following sensitivity experiments, which are summarized in Table 1.

1. CTRL: The control simulation included all BC aerosol radiative effects and BC aging through physical processes but no BC absorption enhancement.
2. NoBCrad: The same as the CTRL simulation, except that the direct radiative effects of BC were turned off.
3. NoBCaging: The same as the CTRL simulation, except that BC aging through physical processes was turned off. BC particles did not age through the coagulation process and did not grow by the transfer of BC mass between different size bins.
4. NoBCaging&rad: The same as the CTRL simulation, except that both the direct radiative effect and aging physical processes of BC were turned off.
5. CTRL_1.5ab: The same as the CTRL simulation, except that the BC absorption coefficient was amplified by a factor of 1.5.

Table 1
Sensitivity experiments. Y indicates "yes", and N indicates "no". The numbers indicate the amplification factors of the BC light absorption coefficient.

Sensitivity case	BC direct radiative effect	BC physical aging processes	BC absorption coefficient amplification
CTRL	Y	Y	N
NoBCrad	N	Y	N
NoBCaging	Y	N	N
NoBCaging&rad	N	N	N
CTRL_1.5ab	Y	Y	1.5

The direct radiative effect of BC was turned off in the NoBCrad simulation by setting the BC mass concentration to zero when calculating the optical properties of BC as described in Qiu et al. (2017) and Gao et al. (2018). BC aging through physical processes of BC was turned off by skipping the BC coagulation process and the BC mass transfer process between different size bins. One new variable was allocated to store the BC mass before passing to the coagulation and mass transfer subroutines in WRF-Chem, and this variable was used to overwrite the BC mass updated by these subroutines. This method ensured that the BC mass would not be changed by these two processes. During periods of heavy pollution, BC is often coated with inorganic and organic materials through coagulation, heterogeneous phase reaction and condensation processes (Moteki et al., 2007; Laborde et al., 2013). Theoretically, the light absorption properties of BC can be enhanced by a factor of 1.0– 2.4 by the coating, which acts as a lens (Jacobson, 2001; Cappa et al., 2012; Q. Wang et al., 2014; Peng et al., 2016). To better simulate the direct radiative effect of BC during this heavy pollution event in the BTH region, we enlarged the absorption coefficient of BC by a factor of 1.5 in CTRL_1.5ab. The AE used in this study was based on previously measured AE values over the BTH region, as summarized in Table 2. In some current climate models, AE is also assumed to be a constant value of approximately 1.5 (Flanner et al., 2007; Bond et al., 2013; Q. Q. Wang et al., 2014).

To avoid the direct radiative feedback from BC, we used NoBCrad and NoBCaging&rad to examine the effects of physical BC aging processes on the mass concentration and particle size distribution of BC. The difference in the model results between NoBCaging and NoBCaging&rad (NoBCaging minus NoBCaging&rad) represents the direct radiative effect of BC without PP and AE. The difference between CTRL and NoBCaging&rad (CTRL minus NoBCaging&rad) represents the direct radiative effect of BC with PP but without AE. The direct radiative effect of BC with both PP and AE is quantified as the difference between CTRL_1.5ab and NoBCaging&rad (CTRL_1.5ab minus NoBCaging&rad). For all simulations, the model was first spun up for 64 h followed by the analysed time period. We used local time in this study unless stated otherwise.

In this study, we applied integrated process rate (IPR) analysis to quantify the changes in O_3 caused by the radiative impact of BC without PP and AE, without AE, and with PP and AE. The IPR analysis in the WRF-Chem model characterizes O_3 with five different processes, namely, sub-grid convection (CONV), chemistry (CHEM), vertical mixing (VMIX), horizontal advection (ADVH), and vertical advection (ADVZ). CHEM represents O_3 chemical production and loss. VMIX is affected by atmospheric turbulence (Zhang and Rao, 1999; Gao et al., 2017). ADVH and ADVZ are largely determined by horizontal and vertical O_3 concentration gradients, respectively, and by winds (Gao et al., 2018; Chen et al., 2019). IPR analysis has been widely applied to study the impacts of physical/chemical processes on O_3 pollution (Xing et al., 2017; Tang et al., 2017; Gao et al., 2018).

Table 2
A summary of the measured absorption enhancements (AE) from previous studies.

Location	Sampling period	Measurement technique[a]	AE	λ (nm)[b]	Reference
Beijing, China	August–October 2013	AMS, PAX	**1.0–2.4**	405, 532	Peng et al., 2016
Beijing, China	9–27 January 2013	SP2	**1.22–1.24**	870	Wu et al., 2016
Yucheng, China	June–July 2014	EC/OC analyser	**2.25 ± 0.55**	678	Cui et al., 2016
Beijing, China	November–December 2016, May–June 2017	SP2, SP-AMS	**1.25–1.70**	550	Liu et al., 2019
Beijing, China	April and September 2018	SP2	**1.1–1.9**	550	S. Ding et al., 2019
Beijing, China	4 June-13 June 2017	SP-AMS, CAPS PM_{ssa}, SP2	**1.59 ± 0.26**	630	Xie et al., 2019
Beijing, China	December 2016	SP2	**1.3–1.7**	550	Zhao et al., 2019
Beijing, China	25–27 November 2018	SP2	**1.4–1.9**	550	Zhao et al., 2020

[a] AMS: aerosol mass spectrometer; PAX: photoacoustic extinctiometer; SP2: single-particle soot photometer; SP-AMS: thermodenuder coupled with a soot particle aerosol mass spectrometer; CAPS PM_{ssa}: cavity attenuated phase shift single scattering albedo monitor.
[b] λ means the wavelength light.

2.4. Observation data

The hourly temperature at 2 m (T2), relative humidity at 2 m (RH2), wind speed at 10 m (WS10) and wind direction at 10 m (WD10) at 20 stations were obtained from NOAA's National Climatic Data Center (http://gis.ncdc.noaa.gov/maps/ncei/cdo/hourly). The 3-hourly PBLH observations for Beijing were obtained from the Global Data Assimilation System (GDAS) (http://ready.arl.noaa.gov/READYamet.php). We also employed vertical profiles of temperature (T) at 8:00 and 20:00 local time in Beijing obtained from the Department of Atmospheric Science at the University of Wyoming (http://weather.uwyo.edu/). To evaluate the performance of the model in simulating pollutants during the haze event in the BTH region, hourly observed concentrations of $PM_{2.5}$ and O_3 in 40 cities were collected from the China National Environmental Monitoring Center (http://www.cnemc.cn). The hourly BC concentrations were collected by the Tower Division of the Institute of Atmospheric Physics, Chinese Academy of Sciences in Beijing using a single-particle soot photometer (SP2) from 21 to 27 February 2014. The aerosol optical depth (AOD) at 550 nm retrieved from the Moderate Resolution Imaging Spectroradiometer (MODIS, https://ladsweb.modaps.eosdis.nasa.gov/) of the Aqua and Terra satellites was used to evaluate the performance of WRF-Chem in simulating the optical properties of aerosols in this study.

3. Model evaluation

3.1. Evaluation of meteorological parameters

During the haze event, the western and northern parts of BTH were dominated by westerly winds, while the southern part was dominated by weak southerly and southwesterly winds associated with high pressure to the east of BTH (Fig. S2). The southerly and southwesterly winds transported pollutants from the southern NCP to the northern NCP and caused aerosols and air pollutants to accumulate in central BTH. Fig. 1 shows the 3-hourly observational and simulated T2, RH2, WS10 and WD10 averaged over 20 stations during 21–27 February 2014. The correlation coefficient (R), mean bias (MB), normalized mean bias (NMB) and mean fractional error (MFE) were calculated and are summarized in Table 3. The temporal correlation coefficients between the simulated and observed T2 and RH2 were both greater than 0.9, while R decreased

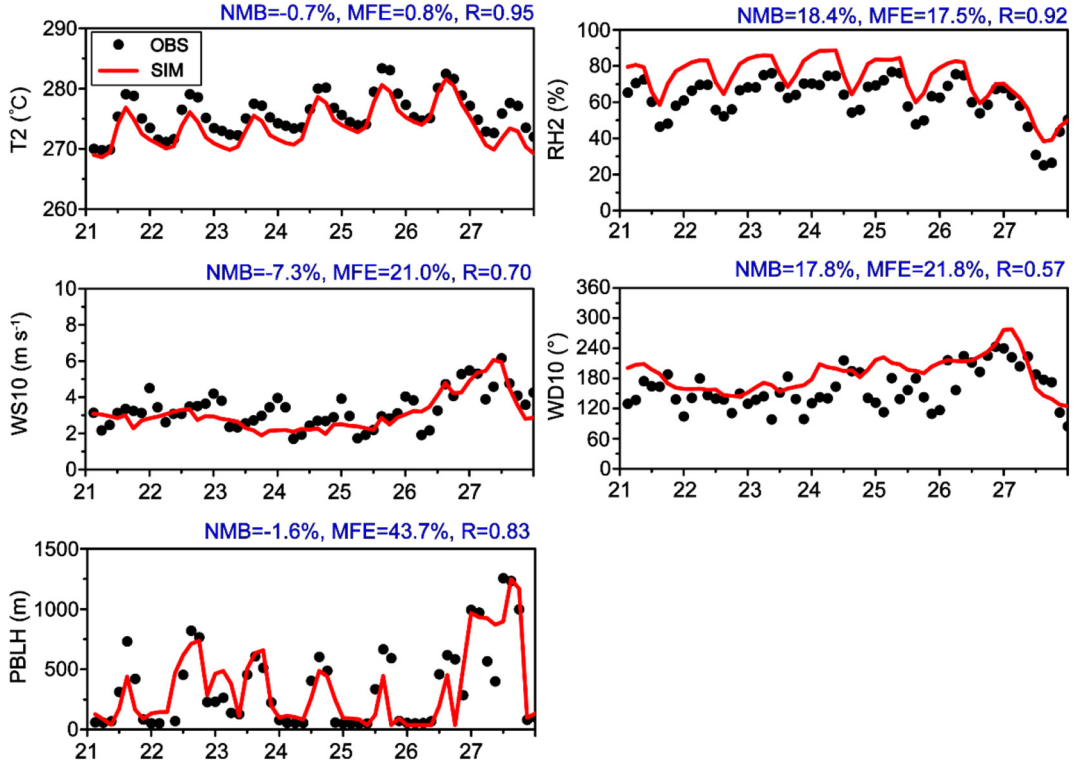

Fig. 1. The black dots and red solid lines are the 3-hourly observed and hourly simulated data, respectively, for the temperature (°C) at 2 m, relative humidity (%) at 2 m, and wind speed ($m\ s^{-1}$) and wind direction (°) at 10 m. Data are averaged over 20 stations in BTH from 21 to 27 February 2014 except that the observed and simulated PBLH (m) data are only at the site in Beijing (39.93°N, 116.28°E). (For interpretation of the references to colour in this figure legend, the reader is referred to the web version of this article.)

Table 3
Correlation coefficients (R), mean bias (MB), normalized mean bias (NMB) and mean fractional error (MFE) of the simulated temperature at 2 m (T2; °C), relative humidity at 2 m (RH2; %), wind speed at 10 m (WS; m s^{-1}), wind direction at 10 m (WD; °) and planetary boundary layer height (PBLH; m) compared with the observations averaged over the 20 stations in BTH from 21 to 27 February 2014.

Variable	n	OBS[a]	SIM[a]	R[b]	MB[c]	NMB[d]	MFE[e]
T2 (K)	20	275.7	273.7	0.95	−2.1	−0.7	0.8
RH2 (%)	20	61.5	72.9	0.92	11.3	18.4	17.5
WS10 (m s^{-1})	20	3.3	3.1	0.70	−0.2	−7.3	21.0
WD (°)	20	159.9	188.4	**0.57**	28.4	17.8	21.8
PBLH (m)	1	348.7	343.0	0.83	−5.7	−1.6	**43.7**

[a] SIM and OBS represent the average simulation and observation values, respectively, from 21 to 27 February 2014.

[b] R is the correlation coefficient calculated between the hourly observations and simulations in Beijing from 21 to 27 February 2014, $R = \frac{\sum_{i=1}^{n}((OBS_i - \overline{OBS}) \times (SIM_i - \overline{SIM}))}{\sqrt{\sum_{i=1}^{n}(OBS_i - \overline{OBS})^2 \times \sum_{i=1}^{n}(SIM_i - \overline{SIM})^2}}$, where OBS^i and SIM^i are the hourly observed and simulated data and n is the total number of hours.

[c] $MB = \frac{1}{n} \times \sum_{i=1}^{n}(SIM_i - OBS_i)$.

[d] $NMB = \frac{\sum_{i=1}^{n}(SIM_i - OBS_i)}{\sum_{i=1}^{n} OBS_i} \times 100\%$.

[e] $MFE = \frac{2}{n} * \sum_{i=1}^{n} \frac{|SIM_i - OBS_i|}{SIM_i + OBS_i} \times 100\%$.

to approximately 0.7 for WS10 and 0.6 for WD10. The model reasonably captured the temporal variations in surface temperature, relative humidity, wind speed and wind direction at the 20 stations. Compared to the observations, the model slightly underestimated T2, with an MB and NMB of −2.1 K and − 0.7%, respectively. During 21–27 February 2014, the observed mean RH2 exceeded 60%, and WS10 was less than 4 m s^{-1}, which favoured the formation of secondary aerosols (e.g., sulfate and nitrate) and the accumulation of pollutants in the BTH region (Sun et al., 2006; Q. Wang et al., 2014). The RH2 values were consistent between the simulations and observations, with absolute biases (MB) of 18.4%. The model captured the observed low WS10 value well, with an NMB and MFE of −7.3% and 21.8%, respectively. The model simulation of the wind direction in the BTH region had NMB and MFE values of −1.6% and 43.7%, respectively.

Due to the limited observational data for PBLH and vertical temperature profiles in the BTH region, we were able to compare the observed and simulated PBLH and temperature vertical profiles during 21–27 February 2014 only in Beijing city (40.0°N, 116.3°E). The model captured diurnal variations in PBLH with R and NMB values of 0.8 and − 1.6%, respectively. Fig. S3 shows the observed and simulated temperature profiles at 8 am and 8 pm in Beijing during 21–27 February 2014. Temperature inversions below 1500 m were observed in Beijing, which was unfavourable for the dispersion of pollutants. The model was able to capture this temperature inversion during the haze event in Beijing.

3.2. Evaluation of atmospheric composition

Fig. S4 shows the horizontal distribution of the observed and simulated daily mean concentrations of $PM_{2.5}$, O_3 and BC in central and eastern China (outer domain d01) averaged during 21–27 February 2014. High concentrations of $PM_{2.5}$ were observed in the BTH region, where the O_3 concentration was relatively low compared to that in the surrounding regions. The maximum value of observed daily $PM_{2.5}$, 498 μg m^{-3}, occurred on February 25 in Tangshan (east of BTH); this value far exceeded the air quality standard of 75 μg m^{-3} in China (Wang et al., 2017). The model captured the spatial distributions of the $PM_{2.5}$ and O_3 concentrations compared to the observed data with spatial R values of 0.68 and 0.53, respectively. Note that some sites were outside the inner domain of the NCP (d02) where the concentrations were affected by lateral boundary conditions, and modelled values over a grid cell can contribute to mismatch bias when comparing to site observations (Chen et al., 2019). Due to the lack of observational BC data, only the spatial distribution of the simulated BC mass concentration is analysed in Fig. S4c. The spatial distribution of the simulated BC concentration was similar to that of $PM_{2.5}$, with high values in the BTH region. Ji et al. (2017) reported that BC accounted for approximately 4.0% of the $PM_{2.5}$ concentration during heavy pollution events in Beijing. Fig. S3d–e shows scatterplots of the simulated versus observed daily $PM_{2.5}$ and O_3 concentrations in the 40 cities marked in Fig. S4a–b. The model slightly underestimated the concentrations of $PM_{2.5}$, with an NMB of −9.2%, while the model overestimated the O_3 concentrations at most of the sites, with an NMB of 13.5%. The model performed well in simulating the spatial distributions of the $PM_{2.5}$ and O_3 concentrations during 21–27 February in central eastern China.

We selected Beijing, Tianjin and three cities in Hebei Province (Shijiazhuang, Zhangjiakou and Chengde) for evaluations of the simulated time series of the $PM_{2.5}$, O_3, and BC concentrations against observations during the haze event, as shown in Fig. 2. The corresponding statistical metrics are summarized in Table 4. The model reproduced the temporal variations in $PM_{2.5}$ in the five cities during the haze event with correlation coefficients (R) between the simulated and observed hourly concentrations of 0.83, 0.85, 0.68, 0.69 and 0.83 for Beijing, Tianjin, Shijiazhuang, Zhangjiakou and Chengde, respectively. Compared to the observations, the simulated concentrations of $PM_{2.5}$ in Beijing, Shijiazhuang and Zhangjiakou were underestimated by 25.9 μg m^{-3} (11.4%), 29.0 μg m^{-3} (9.7%) and 1.0 μg m^{-3} (0.4%), respectively, while those in Tianjin and Chengde were overestimated by 23.0 μg m^{-3} (13.0%) and 0.3 μg m^{-3} (0.2%), respectively. The simulated and observed concentrations of O_3 both showed obvious diurnal variations in the five cities, with the peak O_3 concentrations occurring at noon. The diurnal variations in O_3 were mainly driven by the influence of photochemical reactions, while $PM_{2.5}$ was primarily affected by PBL height and local emissions. The model overestimated the O_3 concentrations in five cities with MB (NMB) values of 2.7 ppbv (33.3%), 1.9 ppbv (19.2%), 0.8 ppbv (8.0%), 2.8 ppbv (23.2%) and 0.9 ppbv (6.4%). In Beijing, changes in BC over time from February 21–27 were well simulated, with a correlation coefficient (R) of 0.83 between the simulated and observed BC and an MB (NMB) of 3.9 μg m^{-3} (49.8%). The model overestimated the mass concentration of BC, which is consistent with Qiu et al. (2017).

3.3. Evaluation of aerosol optical depth

The aerosol optical depth (AOD) is a measure of column-integrated aerosol loading that largely determines the direct radiative effect of aerosols. In WRF-Chem, the optical properties of aerosols are calculated only at specific wavelengths (300 nm, 400 nm, 600 nm, and 1000 nm), whereas the observed AOD obtained from the MODIS satellite is at 550 nm. To evaluate the performance of the model in simulating AOD, we derived the simulated AOD at 550 nm using Eqs. (1) and (2) (Schuster et al., 2006). We first calculated the Angstrom coefficient (α) through Eq. (1), where AOD_{400} and AOD_{600} are the simulated AOD at wavelengths of 400 nm and 600 nm, respectively, and λ_{400} and λ_{600} are the 400 nm and 600 nm wavelengths, respectively. Then, the AOD at 550 nm was calculated with Eq. (2). The observed AOD at 550 nm represents the daily average for the satellite data.

$$\alpha = \left[\frac{\ln \frac{AOD_{400}}{AOD_{600}}}{\ln \frac{\lambda_{400}}{\lambda_{600}}} \right] \quad (1)$$

$$AOD_{550} = AOD_{400} \times \left(\frac{\lambda_{550}}{\lambda_{400}} \right)^{-\alpha} \quad (2)$$

Fig. S5 shows the horizontal distribution of the simulated and observed AOD in NCP during the haze event. The high-value centre of AOD was located in the BTH region and corresponded to the area with high $PM_{2.5}$ concentrations (Fig. S4a). The model simulates the spatial

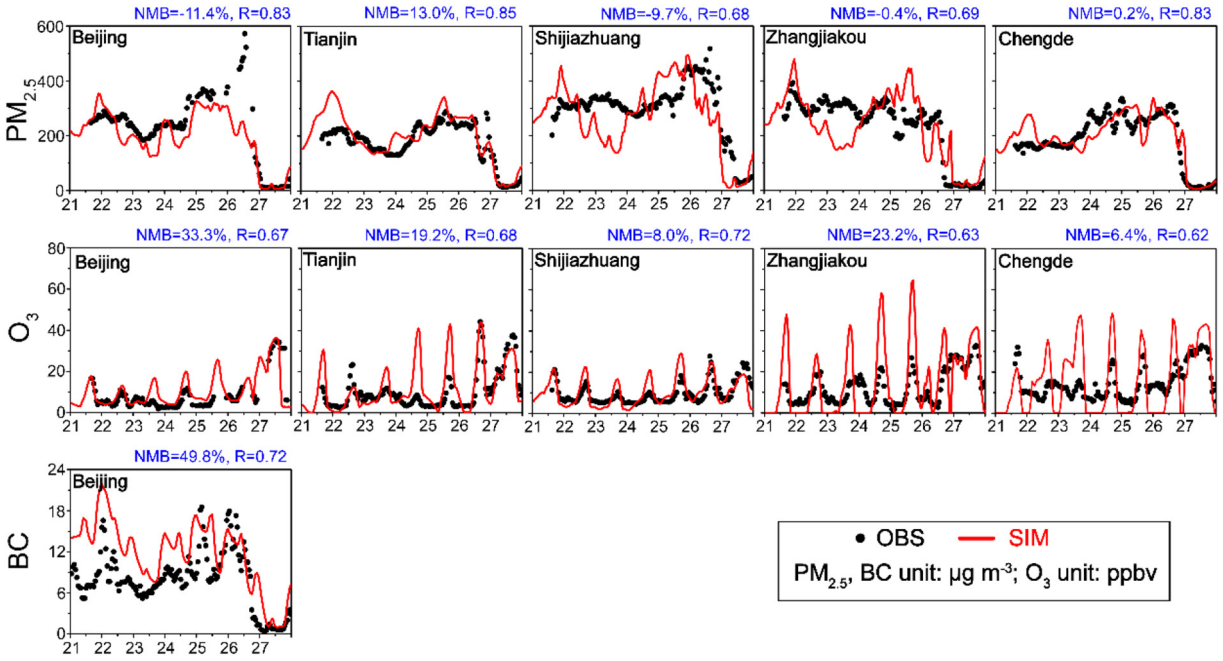

Fig. 2. Time series of simulated (red solid lines; CTRL simulation) and observed (black dots) hourly mass concentrations of $PM_{2.5}$ (μg m^{-3}), O_3 (ppbv) and BC (μg m^{-3}) in five cities (Beijing, Tianjin, Shijiazhuang, Zhangjiakou and Chengde) during 21–27 February 2014. (For interpretation of the references to colour in this figure legend, the reader is referred to the web version of this article.)

distribution of AOD in NCP well, with a spatial correlation coefficient of 0.91. However, in the heavily polluted area of the BTH region, AOD was significantly underestimated by the model. The observed AOD value in BTH was 2.16 during 21–27 February 2014, while the simulated value was 1.03. Previous studies have shown that MODIS retrieval tends to overestimate the AOD in severe pollution events in northern China (Li et al., 2016). On the other hand, the internal mixing assumption, fixed refractive indices, and lack of BC absorption enhancement in the WRF-Chem model partly explain the low bias (Curci et al., 2014).

4. Changes in BC concentration and size due to aging physical processes

To quantitatively characterize the aging physical processes of BC during the heavy pollution event in the BTH region, the simulated concentrations of BC mass in the eight size bins were modelled with NoBCrad and NoBCaging&rad and are shown in Fig. 3. These two sensitivity experiments both removed the direct radiative effect of BC. The BC concentrations with and without PP in all bins decreased with height in the BTH region. Aging by PP did not change the vertical distribution of the exponential decline in BC with height, but it did change the BC concentration in each bin. Near the surface, PP reduced the BC concentrations by 2.1 μg m^{-3} (84.9%), 0.7 μg m^{-3} (42.7%) and 0.2 μg m^{-3} (6.2%) in bin 1, bin 2 and bin 3, respectively, but increased the BC concentrations by 1.6 μg m^{-3} (65.1%), 0.6 μg m^{-3} (75.6%) and 0.1 (47.9%) in bin 4, bin 5 and bins 6–8, respectively, averaged over the BTH during 21–27 February 2014. The total concentration of near-surface BC was reduced by 0.7 μg m^{-3} (6.6%) in the BTH region with PP because the larger aged hydrophilic BC particles can be more effectively removed by scavenging and sedimentation than the smaller particles. Fig. 3c shows that at different heights, the PP similarly reduced the BC concentrations in the small particle size bins (bins 1, 2 and 3) but increased the concentrations in the larger size bins (bins 4, 5 and 6–8).

Fig. 3d–e illustrates the vertical profiles of the fractions of the BC concentrations (with and without PP) in the individual size bins relative to the corresponding total BC concentrations averaged over BTH during 21–27 February 2014. Previous studies have revealed that BC aging processes can strongly affect BC particle size (Liu et al., 2014; Takahama et al., 2014). In WRF-Chem, fresh BC particles are initially emitted into the eight size bins by mass fractions of 14.5%, 8.9%, 26.4%, 32.53%, 10%, 7.5%, 0.4%, and 0%, respectively, from bin 1 to bin 8. In the BTH region, when PP were not considered, the proportion of the BC concentration in bin 3 was the largest below 1000 m, with a fraction range of 26.1–27.9%, followed by 23.8–26.9% in bin 1, 19.8–23.3% in bin 4 and 15.6–19.1% in bin 2. Bins 5–8 together accounted for 8.0–9.4%. However, when PP were considered, the proportion of the BC concentration in the larger particle-size bins increased substantially below 1000 m; the proportions in bin 4 and bins 5–8 increased to 41.2–44.7% and 17.3–19.4%, respectively, while the proportions in bin 1 and bin 2 decreased from 23.8–26.9% and 15.6–19.1% to 1.4–3.8% and 7.3–9.5%, respectively. When aging PP were turned off, the proportion of BC in the small particle-size bins (1 and 2) gradually increased with height, and that in the large particle-size bins (3–8) decreased as the height increased (Fig. 3e). However, when aging PP were included, with the increase in height, the proportions of BC in bin 4 and bin 5 increased first and then decreased gradually and exhibited a peak at approximately 400 m. These results suggest that the impacts of PP on BC in the lower boundary layer are much greater than the impacts of other physical processes (e.g., dry deposition, wet removal, horizontal and vertical

Table 4
The correlation coefficient (R), mean bias (MB), mean absolute error (MAE), normalized mean bias (NMB) and mean fractional error (MFE) of the simulated $PM_{2.5}$, O_3 and BC compared with the observed data.

	Variable	n	OBS	SIM	R	MB	NMB	MFE
Beijing	$PM_{2.5}$ (μg m^{-3})	12	226.3	200.4	0.83	−25.9	−11.4	27.8
	O_3 (ppbv)	12	8.1	10.8	0.67	2.7	33.3	32.5
	BC (μg m^{-3})	1	7.8	11.8	0.72	3.9	49.8	49.2
Tianjin	$PM_{2.5}$ (μg m^{-3})	10	176.7	199.7	0.85	23.0	13.0	19.3
	O_3 (ppbv)	10	10.0	12.0	0.68	1.9	19.2	40.3
Shijiazhuang	$PM_{2.5}$ (μg m^{-3})	8	298.2	269.2	0.68	−29.0	−9.7	34.2
	O_3 (ppbv)	8	9.5	10.2	0.72	0.8	8.0	39.2
Zhangjiakou	$PM_{2.5}$ (μg m^{-3})	4	233.3	232.3	0.69	−1.0	−0.4	35.1
	O_3 (ppbv)	4	12.3	15.1	0.63	2.8	23.2	45.1
Chengde	$PM_{2.5}$ (μg m^{-3})	8	190.1	190.5	0.83	0.3	0.2	22.7
	O_3 (ppbv)	8	14.4	15.4	0.62	0.9	6.4	47.4

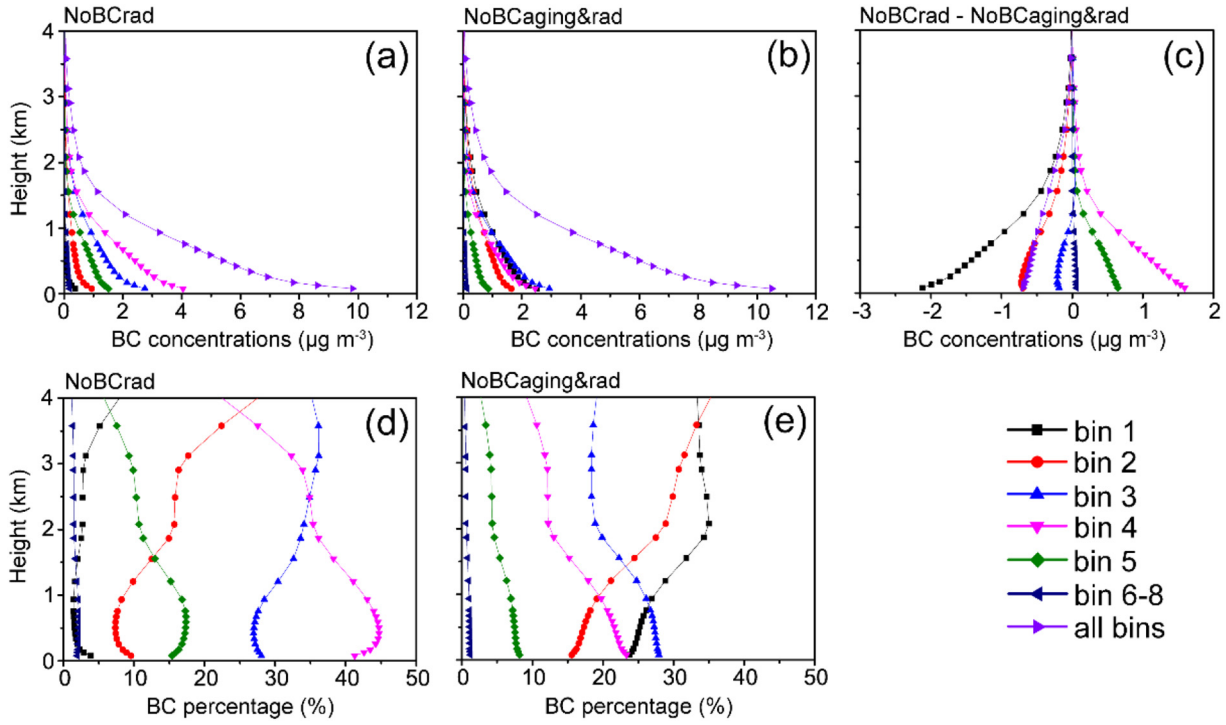

Fig. 3. (a–c) Simulated vertical profiles of the BC mass concentrations (μg m^{-3}) in NoBCrad (with PP) and in NoBCaging&rad (without PP) and their differences (NoBCrad – NoBCaging&rad) in eight size bins averaged over BTH during 21–27 February 2014. (d–e) Vertical profiles of the mass fractions of the BC concentrations (μg m^{-3}) within individual size bins in NoBCrad and in NoBCaging&rad, respectively, for the corresponding total BC concentrations averaged over BTH during 21–27 February 2014.

transportation). Although the total mass concentration of BC was reduced by the aging PP, the mass concentration of large BC was significantly increased. Matsui et al. (2018) reported that the mass absorption cross-section (MAC) of BC particles at a mass median diameter of 0.2 μm was the highest when the model considered only a single BC mixing state (internal mixing). When the BC light absorption enhancement due to the "lensing" effect was considered, the direct radiative effect of BC on meteorological conditions and pollutants became more complicated.

Fig. S6 compares the horizontal distribution of column BC mass loading between NoBCaging&rad and NoBCrad. High BC mass loading appeared in the BTH region regardless of the aging PP. Averaged over 21–27 February 2014 in the BTH region, BC mass loading was 9.1 mg m^{-2} without PP and 8.0 mg m^{-2} with PP. The aging PP did not change the spatial distribution of the BC mass loading, with a spatial correlation coefficient of 0.99, but reduced the magnitude of the BC mass loading over the entire BTH region. Fig. S6c shows the difference in the spatial distribution of the BC mass loading between the simulations with and without PP. The largest difference in mass loading was also observed in the BTH region, with an average decrease of 1.1 mg m^{-2} (12.1%) compared to the results of NoBCaging&rad.

5. Direct radiative effects of BC without PP & AE, without AE and with PP & AE on meteorological conditions and pollutants

In this section, we investigate the interactions between meteorology and BC without PP & AE, without AE and with PP & AE by examining the differences between NoBCaging and NoBCaging&rad, CTRL and NoBCaging&rad, and CTRL_1.5ab and NoBCaging&rad, respectively.

5.1. Direct radiative effect of BC on meteorological conditions

BC can heat the ambient air by absorbing solar radiation, redistributing energy in the vertical direction, and thus influencing meteorological fields. Fig. 4a–f shows the spatial distributions of changes in net radiative fluxes at the surface and at the top of the atmosphere (TOA) due to the different models of BC in NCP averaged over the heavy haze episode. The downward shortwave radiative flux at the surface over the entire NCP was reduced by −10.5 W m^{-2} due to the presence of BC without considering PP and AE, and the magnitude of this effect was increased by 1.3 W m^{-2} (12.4%) and 4.3 W m^{-2} (41.0%) when PP and AE, respectively, were considered in the model. At the TOA, the BC radiative effect increased the net incoming radiation over the NCP by 9.2 W m^{-2}, 10.1 W m^{-2} and 12.9 W m^{-2}, respectively, for the cases without PP & AE, without AE and with PP & AE. Within the BTH region, the mean BC radiative forcing at the surface (SUR), in the atmosphere (ATM) and at TOA for the simulations without PP & AE, without AE, and with PP & AE were − 11.5, 21.1 and 9.5 W m^{-2}, −12.8, 23.3 and 10.8 W m^{-2}, and − 17.7, 31.1 and 13.4 W m^{-2}, respectively, averaged over 21–27 February 2014. Although the PP decreased BC concentrations over BTH, the changes in BC particle size increased their impacts on radiative fluxes at SUR, ATM and TOA. Strong negative SUR forcing and positive ATM forcing can result in cooling at the surface and warming in the atmosphere. The inclusion of both PP and AE strengthened the effect of BC on atmospheric stratification. However, compared to the effect of PP, the effect of AE on BC radiative forcing was larger.

Fig. 5a–c shows the changes in the vertical temperature profile caused by BC heating averaged over the BTH region and during 21–27 February 2014. BC significantly heated the atmosphere, especially in the altitude range of 700–1400 m during 14:00–18:00, with maximum temperature increases of 0.9, 1.1 and 1.4 °C in the simulations without PP & AE, without AE, and with PP & AE, respectively. BC had a slight warming effect at the surface, with increases in surface air temperature of 0.3 °C in all simulations. Although the mass concentration of the near-surface BC was the highest, the largest temperature increase occurred at the top of the PBL (approximately 600–900 m); this increase was due to the stronger shortwave absorption efficiency of the unit mass of BC at higher altitudes (Fig. S7). This is consistent with the results of many previous observational and modelling studies (Samset and Myhre, 2011; Ferrero et al., 2014; Samset et al., 2014; Ding et al., 2016). When the

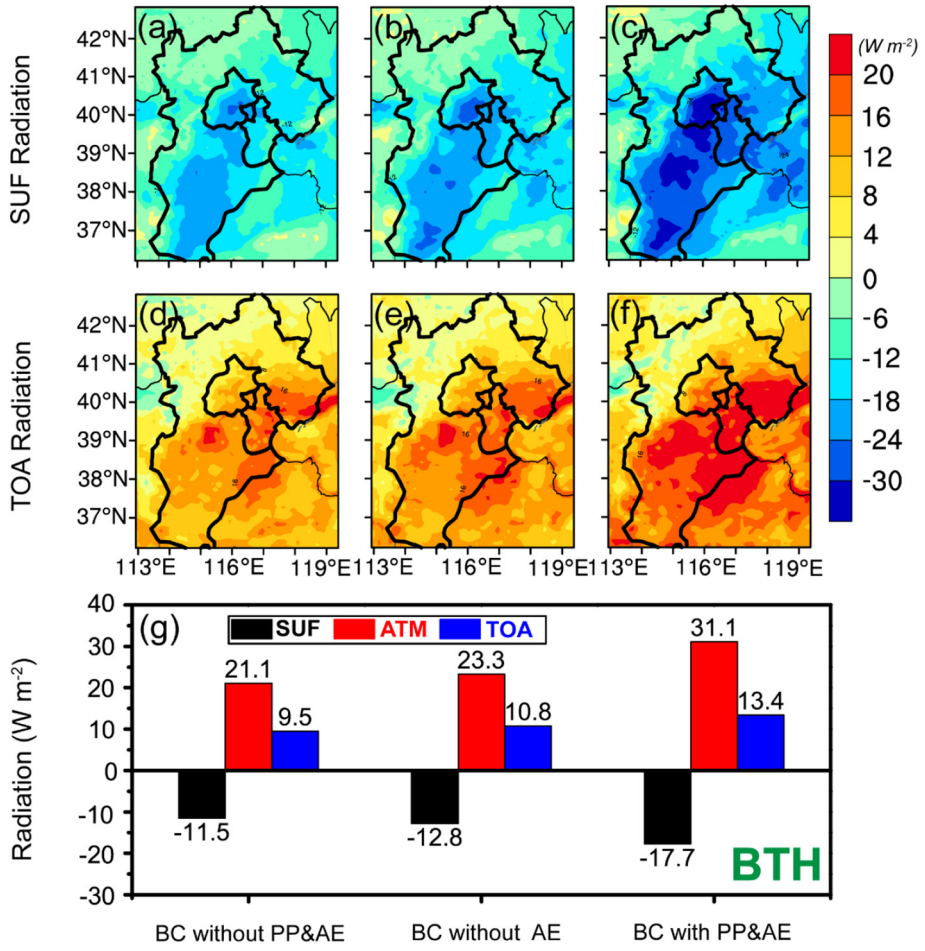

Fig. 4. (a–f) Spatial distributions of changes in radiative fluxes at the surface (SUR; W m^{-2}) and at the top of the atmosphere (TOA; W m^{-2}) due to the direct radiative effect of BC without PP and AE (a and d; NoBCaging – NoBCaging&rad), without AE (b and e; CTRL – NoBCaging&rad), and with PP and AE (c and f; CTRL_1.5ab – NoBCaging&rad) averaged over 21–27 February 2014. (g) Direct radiative effect of BC at the surface, in the atmosphere (ATM) and at TOA averaged over 21–27 February 2014 in the BTH region.

direct radiative forcing of BC was not considered, the simulated PBL was the highest, with a value of 297.1 m averaged over the BTH region during 21–27 February 2014. The strong increase in temperature above the PBL increased the atmospheric stability and suppressed the development of the PBL. Corresponding to the daily maximum temperature changes (14:00–19:00) (Fig. 5a–c), Fig. 5d shows the collocated maximum decreases in the PBL height corresponding to the daily maximum temperature changes (14:00–19:00) caused by BC (Fig. 5a–c). The minimum change in PBL height occurred without PP & AE. In the time period 14:00–19:00, BC effects reduced the PBL height by 66.6 m (11.9%), 75.7 m (13.5%) and 116.3 m (20.7%), respectively, compared to the PBL height in NoBCaging&rad. These results suggest the importance of direct radiative forcing from BC in PBL meteorology. However, at night (22:00–9:00), the PBL height was slightly increased by BC effects; this occurred due to an increase in the surface buoyancy flux driven by daytime BC warming near the ground (Barbaro et al., 2014; Huang et al., 2015; Wang et al., 2018).

Fig. 6 shows the spatial distributions in the changes in PBL height, T2, RH2 and wind at 10 m due to the direct radiative effect of the BC without PP & AE, without AE, and with PP & AE, respectively, averaged over the NCP during 21–27 February 2014. The simulated T2 slightly decreased in the central area of BTH and increased in other areas due to the BC effect when PP & AE were not considered. PP and AE both strengthened the radiative effect of BC on T2. BC effects without PP & AE, without AE, and with PP & AE decreased the mean RH2 over BTH by 1.0%, 1.2% and 1.1%, respectively. The decrease in RH2 likely resulted in a decrease in the concentration of $PM_{2.5}$ produced by chemical reactions. Compared to the baseline in NoBCaging&rad, the BC effect without considering PP & AE (in NoBCaging) induced strong anomalous northeasterly winds from the sea and from relatively clean areas in the eastern NCP, while PP and AE both strengthened the anomalous northeasterly. These changes in wind patterns can be explained by the different heating and cooling effects of BC on the air column and the surface over the NCP region. Similar changes in PBL height, T2, RH2 and wind at 10 m caused by BC were also reported by Qiu et al. (2017) and Gao et al. (2016).

5.2. Impacts of BC on $PM_{2.5}$ and O_3 concentrations

As discussed above, the radiative effect of BC disrupted meteorological variables (such as temperature, PBL, RH2 and wind) in the BTH region during this haze event. Such disruptions can have an impact on $PM_{2.5}$ and O_3 concentrations, which are mainly controlled by meteorological conditions during haze events (Yang et al., 2016). Previous studies have shown that BC significantly changed the near-surface concentration of pollutants by affecting the PBLH (Gao et al., 2016; Ding et al., 2016; Qiu et al., 2017; Gao et al., 2018). Since BC effects during this haze event caused increases or decreases in the PBLH depending mostly on the local time in the BTH region (as shown in Fig. 5), we separately discuss the impacts of BC on near-surface pollutants for the increased and decreased PBLH.

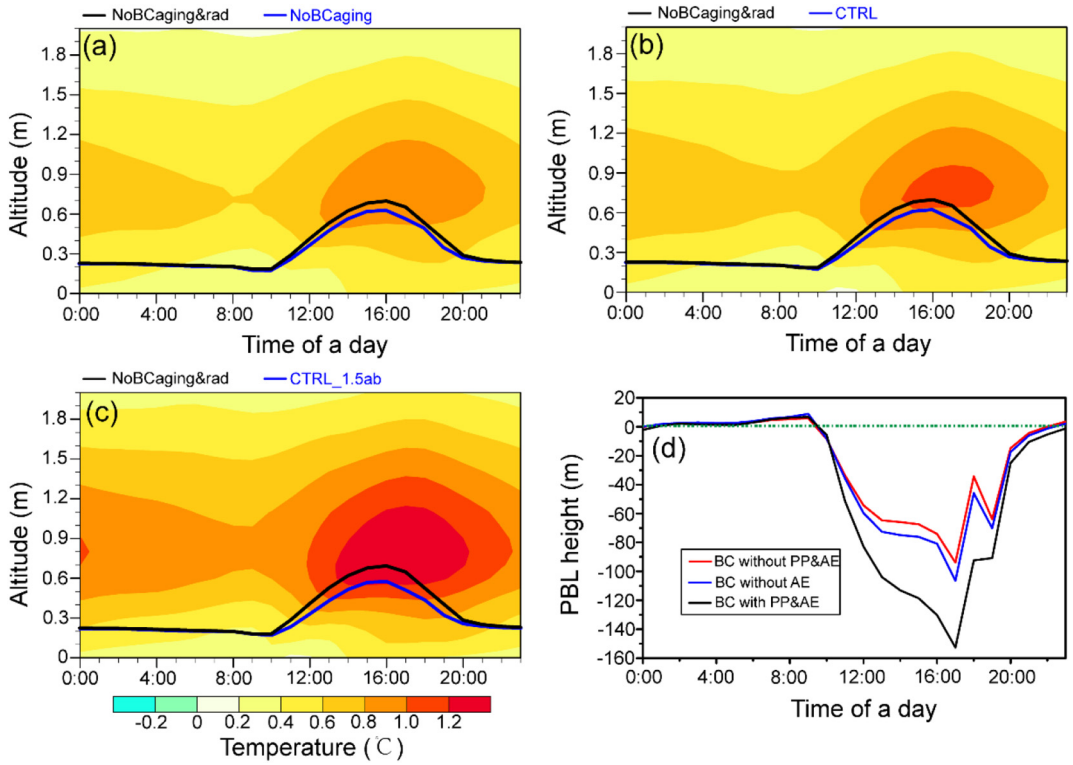

Fig. 5. (a–c) Modelled diurnal variations in temperature (°C) caused by the direct radiative effect of BC (a) without PP and AE, (b) without AE, and (c) with PP and AE in the BTH region during haze days. The overlaid lines are the PBL heights (m) simulated in the four sensitivity experiments. (d) Diurnal variations in the differences in PBL height between NoBCaging and NoBCaging&rad (NoBCaging – NoBCaging&rad; red line), CTRL and NoBCaging&rad (CTRL – NoBCaging&rad; blue line), and CTRL_1.5ab and NoBCaging&rad (CTRL_1.5ab – NoBCaging&rad; black line) in the BTH region on hazy days. The green dotted line indicates zero difference. (For interpretation of the references to colour in this figure legend, the reader is referred to the web version of this article.)

Fig. 7 shows the spatial distributions of changes in near-surface $PM_{2.5}$ and O_3 due to BC without PP & AE, without AE, and with PP & AE for the increased and decreased PBLH averaged over 21–27 February 2014. When the PBLH increased, BC had different effects on $PM_{2.5}$ in the eastern and western parts of BTH. The BC effects without PP & AE, without AE and with PP & AE increased the surface $PM_{2.5}$ concentration by 11.2 μg m^{-3} (12.5%), 11.2 μg m^{-3} (12.5%) and 15.2 μg m^{-3} (16.9%), respectively, in the western part of BTH but reduced it by 13.8 μg m^{-3} (6.6%), 15.9 μg m^{-3} (7.6%) and 21.2 μg m^{-3} (10.2%) in the eastern part. Although the PBLH increased slightly in BTH, anomalous northeasterly winds were produced in the eastern NCP due to BC radiative effects, which accelerated the transport of aerosols and led to a decrease in $PM_{2.5}$ concentrations in the eastern part of BTH. The impact of BC on the $PM_{2.5}$ in BTH under this condition (the increased PBLH) occurred mainly through the change in the wind field. When the PBLH decreased, the near-surface $PM_{2.5}$ concentration increased by 11.4 μg m^{-3} (10.6%), 10.6 μg m^{-3} (9.8%) and 13.7 μg m^{-3} (12.7%) in most areas of the BTH region due to the effects BC without PP & AE, without AE and with PP & AE, respectively. A sharp decrease in PBLH resulted in the accumulation of near-surface $PM_{2.5}$, which outweighed the decrease in $PM_{2.5}$ caused by wind field anomalies in the eastern BTH region.

Tropospheric ozone is a typical secondary pollutant produced mainly by photochemical reactions (Crutzen, 1973). The effects of BC without PP & AE, without AE and with PP & AE reduced the simulated surface O_3 concentrations in most areas of the BTH by mean values of 1.8 ppbv (9.1%), 2.0 ppbv (10.2%) and 1.9 ppbv (9.6%), respectively, when the PBLH increased. Dickerson et al. (1997) reported that BC reduced the surface O_3 concentration by reducing photolysis rates, but the positive ΔPBLH occurred at night, so BC had a weak effect on O_3 under this PBLH condition. When the PBLH was decreased, the mean near-surface O_3 concentration in BTH decreased by 2.8 ppbv (7.4%), 4.0 ppbv (9.0%) and 5.0 ppbv (10.8%) due to the effects of BC without PP & AE, without AE and with PP & AE, respectively. The maximum reductions appeared in the Beijing area. We further analysed the changes in O_3 concentration in BTH from 10:00 to 17:00 caused by the effects of BC without PP & AE, without AE and with PP & AE using IPR analysis, as shown in Fig. 8. Among the contributions of the O_3 processes in the three simulations (NoBCaging, CTRL and CTRL_1.5ab), from 10:00 to 17:00, VMIX made the largest positive contribution to near-surface O_3 and reached its highest values of 6.7 ppbv h^{-1}, 6.5 ppbv h^{-1} and 6.2 ppbv h^{-1}, respectively, between 12:00–13:00 (corresponding to the rapid development of PBL). CHEM made the largest negative contribution to near-surface O_3, and the magnitude of this contribution continued to increase over time in the afternoon. The change in NET in all three simulations showed an increasing trend between 10:00 and 12:00, followed by a decreasing trend. The effects of BC without PP & AE, without AE and with PP & AE influenced the contributions of the O_3 processes, as shown in Fig. 8d–f. The effects of BC caused a reduction in the contribution of VMIX because BC suppressed the development of the PBL and reduced the vertical turbulence, thereby reducing the transport of upper layer O_3 to the surface. The VMIX contribution decreased the most at 10:00 and 17:00, when the PBL developed and decreased rapidly, respectively, and the PBL turbulence changed drastically. Both PP and AE further exacerbated the decrease in VMIX at rates of −0.2 ppbv h^{-1} and −0.5 ppbv h^{-1}, respectively. Because of the decline in the PBLH caused by the effects of BC, a large amount of ozone precursors accumulated within the boundary layer, and the contribution of CHEM to the production of near-surface O_3 increased. Although the positive CHEM offset the negative VMIX to some extent, the NET was still a negative value.

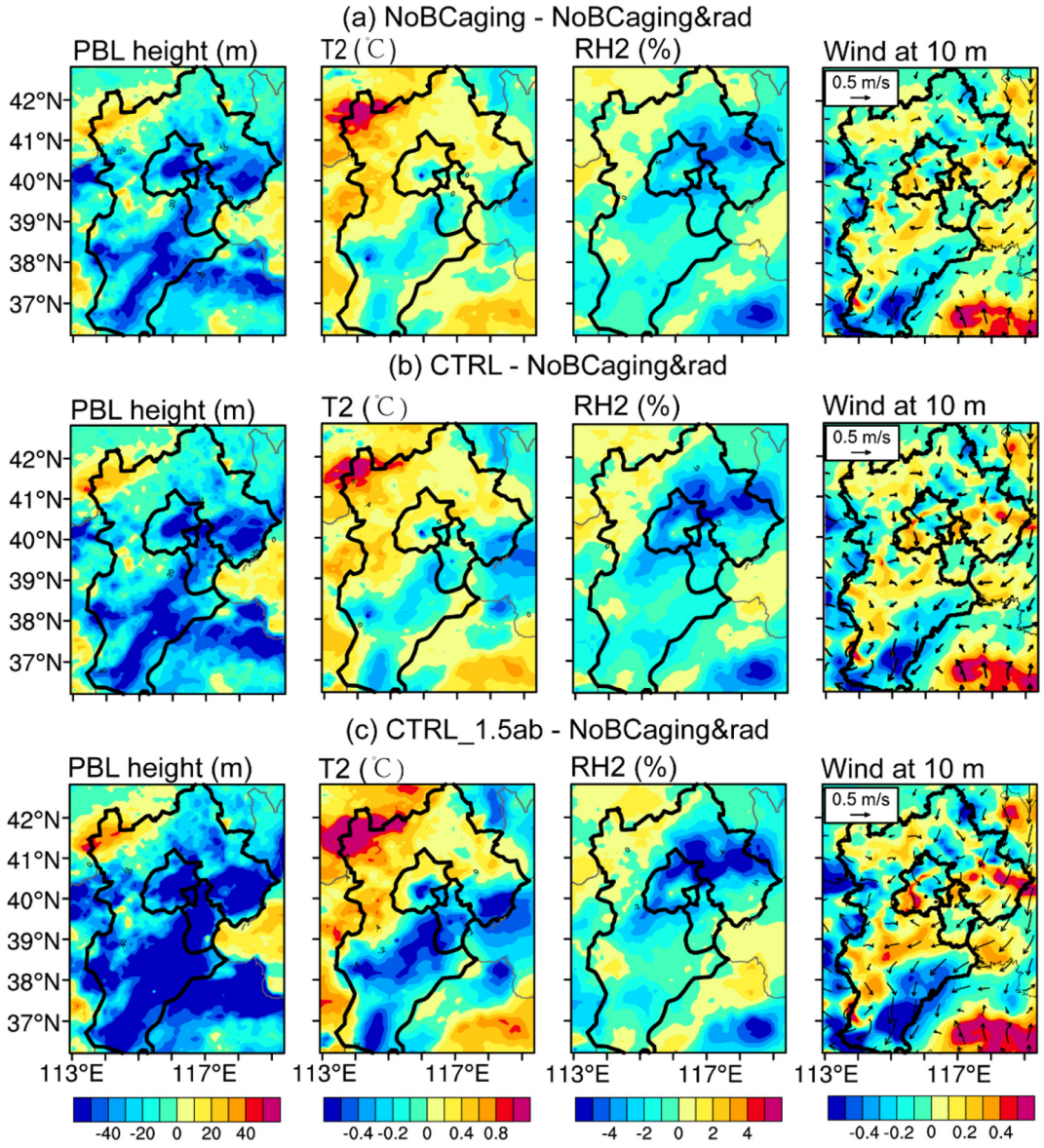

Fig. 6. The spatial distributions of changes in PBL height (m), temperature at 2 m (T2; °C), relative humidity at 2 m (RH2, %) and wind at 10 m due to the direct radiative effect of BC (a) without PP and AE, (b) without AE, and (c) with PP and AE averaged over 21–27 February 2014. The colours in the 10-m wind figures (rightmost column) indicate the corresponding changes in wind speed (m s^{-1}).

6. Conclusion and discussion

In this study, we quantify the impact of BC direct radiative forcing, with the BC aging physical processes (PP) and/or absorption enhancement (AE) turned on/off in the WRF-Chem model, on meteorological variables and air pollutants in BTH during 21–27 February 2014. The temporal correlation coefficients between the simulated and observed surface temperature, relative humidity and wind speed were greater than 0.7 at 20 stations in BTH. The correlation coefficients between the simulated and observed hourly $PM_{2.5}$, O_3 and BC in Beijing were 0.83, 0.67 and 0.72, respectively. The spatial correlation coefficient between the satellite-retrieved AOD and model-simulated AOD over the NCP was 0.91. The comparisons indicate that the WRF-Chem model has the ability to reasonably represent this haze event in the BTH region.

We have demonstrated that the aging PP changed the particle size and mass concentration of BC. The model results show that PP decreased near-surface BC concentrations in size bins 1, 2 and 3 (particle diameters less than 0.312 μm) by 2.1 μg m^{-3} (84.9%), 0.7 μg m^{-3} (42.7%) and 0.2 μg m^{-3} (6.2%), respectively, but increased BC concentrations by 1.6 μg m^{-3} (65.1%), 0.6 μg m^{-3} (75.6%) and 0.1 μg m^{-3} (47.9%) in bin 4, 5 and 6–8, respectively, averaged over the BTH region during this haze event. Overall, the BC aging PP slightly decreased the ground-level BC concentration and the BC column mass loading, by 0.7 μg m^{-3} (6.6%) and 1.1 mg m^{-2} (12.1%), respectively, in BTH. When PP were considered, the proportions of the BC concentrations in the lower atmosphere (below 1000 m) in bins 4–8 increased from 27.8–32.7% to 58.5–64%. We also found that the impact of PP on BC particle size distribution below 500 m is much greater than the combined effects of other physical processes.

Averaged over 21–27 February 2014 in the BTH region, the effects of BC without PP & AE, without AE and with PP & AE reduced downward shortwave radiation at the surface by 11.5 W m^{-2}, 12.8 W m^{-2} and 17.7 W m^{-2} and increased downward shortwave radiation at the top of the atmosphere by 9.5 W m^{-2}, 10.8 W m^{-2} and 13.4 W m^{-2}, respectively. BC significantly heated the atmosphere during 14:00–18:00, especially at altitudes of 700–1400 m, where the air temperature was warmed by 0.9 °C, 1.1 °C and 1.4 °C, respectively. The PBL height was reduced by 66.6 m (11.9%), 75.7 m (13.5%) and 116.3 m (20.7%) from

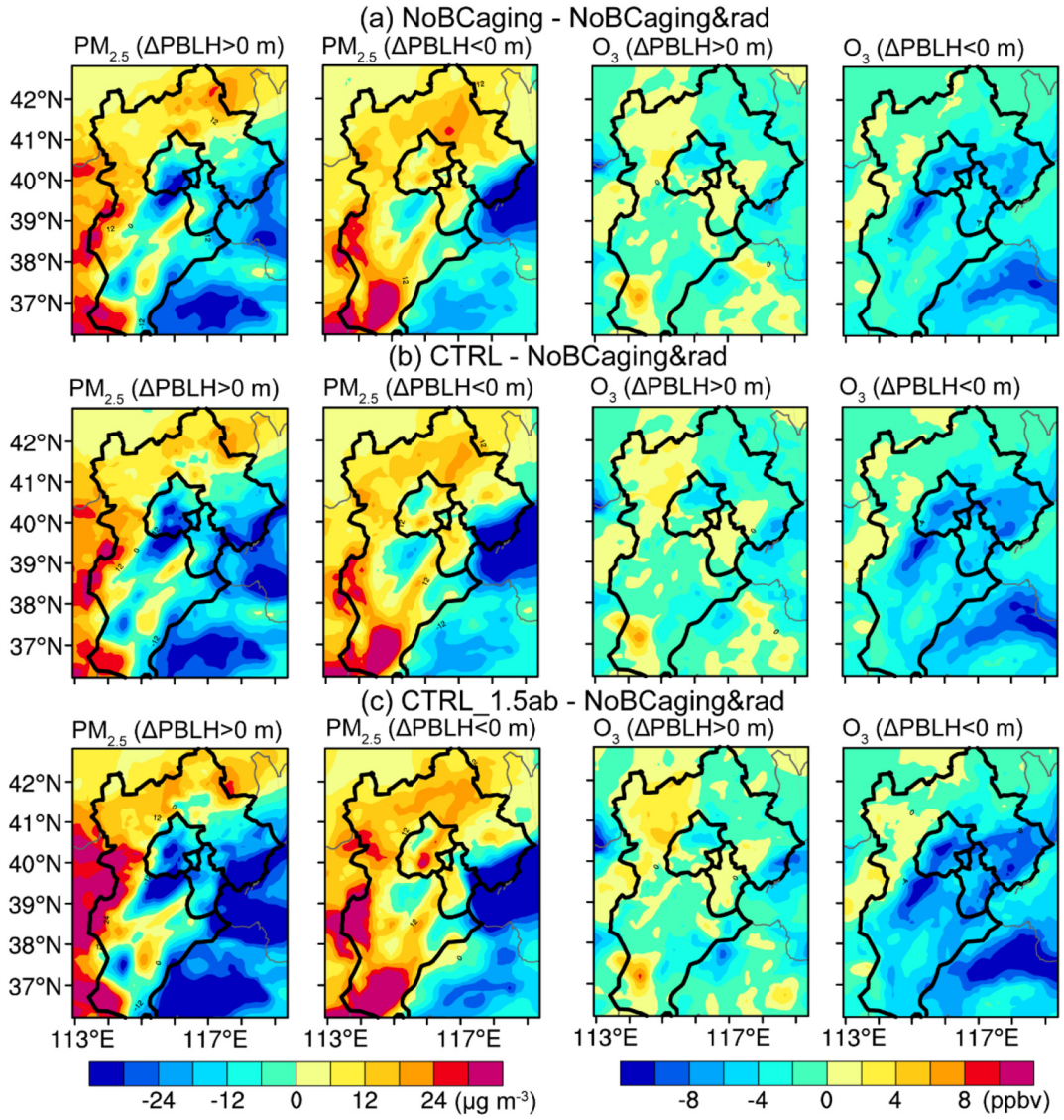

Fig. 7. Spatial distributions of changes in the concentrations of $PM_{2.5}$ and O_3 due to the direct radiative effect of BC (a) without PP and AE, (b) without PP, and (c) with PP and AE averaged over 21–27 February 2014. ΔPBLH >0 m represents the times when the PBLH simulated in the corresponding sensitivity experiment (NoBCaging, CTRL or CTRL_1.5ab) was higher than the PBLH simulated in NoBCaging&rad, and ΔPBLH <0 m represents the opposite situation.

14:00–19:00 due to the effects of BC without PP & AE, with PP and with PP & AE, respectively. However, the PBL height slightly increased from 22:00 to 9:00 at night. On average, over the BTH region from 21 to 27 February 2014, the simulated T2 was slightly reduced in the central NCP and increased in other areas due to the BC radiative effect without PP & AE. PP and AE both strengthened the effect of BC on T2. Relative to the baseline result of NoBCaging&rad, the BC effect over BTH induced strong anomalous northeasterly winds from the ocean and clean-air areas in the eastern NCP, while both PP and AE strengthened the anomalous northeasterly.

Because of the complicated changes in multiple meteorological parameters (temperature, RH2, PBLH and wind field) associated with the BC radiative effect, its impacts on $PM_{2.5}$ and O_3 depended on the time and location in the BTH region. When the PBLH was high, during the daytime, the simulated impact of BC without PP & AE, without AE and with PP & AE increased the surface $PM_{2.5}$ concentration by 11.2 μg m^{-3} (12.5%), 11.2 μg m^{-3} (12.5%) and 15.2 μg m^{-3} (16.9%), respectively, in the western part of the BTH region but decreased the $PM_{2.5}$ concentration by 13.8 μg m^{-3} (6.6%), 15.9 μg m^{-3} (7.6%) and 21.2 μg m^{-3} (10.2%) in the eastern part. When the PBLH is decreased (from 10:00 to 21:00), the near-ground $PM_{2.5}$ concentrations increased by 8.3 μg m^{-3} (6.1%), 6.1 μg m^{-3} (4.5%) and 9.6 μg m^{-3} (7.0%), and the surface O_3 concentration decreased by 2.8 ppbv (7.4%), 4.0 ppbv (9.0%) and 5.0 ppbv (10.8%) in the BTH region due to the effects of BC without PP & AE, without AE and with PP & AE, respectively. Using IPR analysis, we found that VMIX made the largest positive contribution to near-surface O_3, while CHEM made the largest negative contribution. BC reduced the positive contribution of VMIX and the negative contribution of CHEM by suppressing the development of PBL. Both PP and AE strengthened this effect.

In our study, although the model captured the trends of the BC concentrations well, the BC concentrations were overestimated in the simulation, which might have strengthened the modelled direct radiative effects of BC on meteorology and pollutants during this severe haze event. This bias could be related to the uncertainties in the emission inventory and the simulated meteorological parameters (e.g., WD10). As shown in Fig. 1, the model could not completely reproduce the change in WD10 with time in NCP with R of 0.6, which may affect the simulated regional transport of pollutants as well as the simulated BC radiative feedbacks on near-surface $PM_{2.5}$ and O_3.

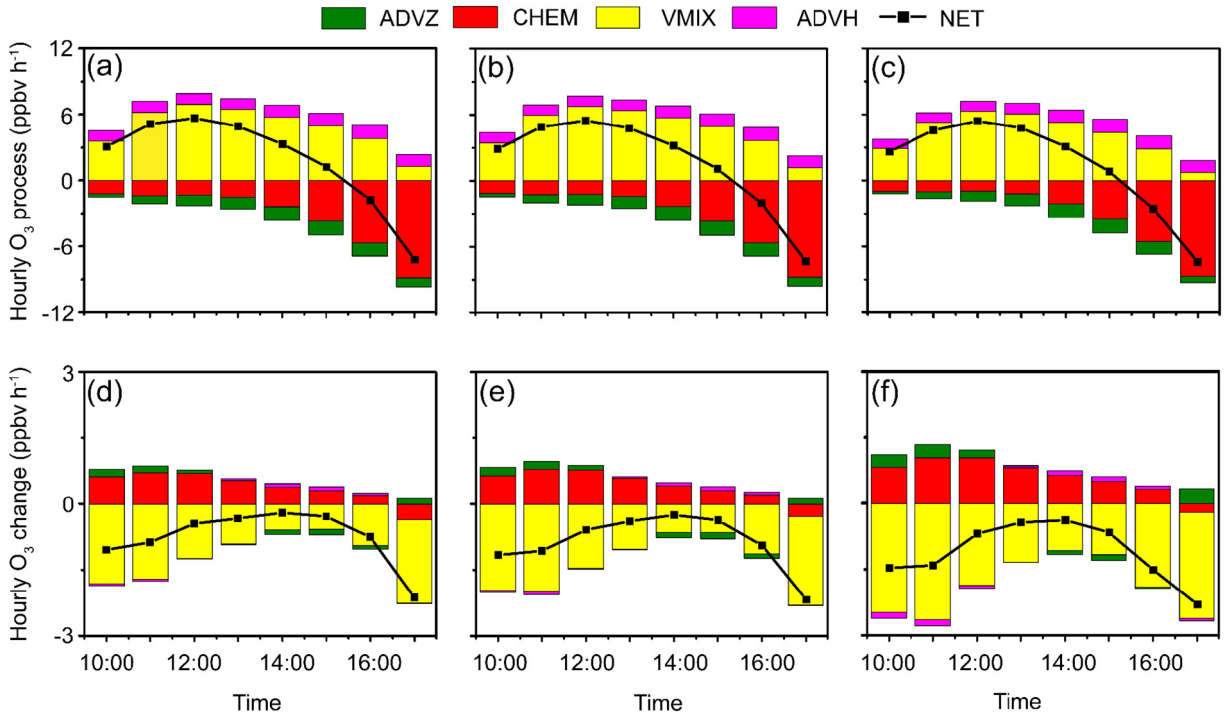

Fig. 8. (a–c) Hourly O_3 process contributions in the NoBCaging, CTRL and CTRL_1.5ab experiments from 10:00 to 17:00 local time. (d–f) Changes in the hourly O_3 process contributions caused by the impact of BC without PP & AE, without AE and with PP & AE, respectively.

A fixed AE value was used in this study due to the lack of sufficient observational BC absorption enhancement data for the NCP area, except for Beijing, during this severe haze event. We adopted a fixed BC absorption enhancement with a value of 1.5 without considering the spatial and temporal variations in AE. Sun et al. (2020) measured BC absorption enhancement at 520 nm in winter in Guangzhou and showed that the AE slightly increased with time during the day and decreased at night. In contrast to this diurnal AE pattern, the fixed AE value we set may have led to an underestimation of the direct radiative effects of BC on meteorology and pollutants during the day and an overestimation of these effects at night during this haze event in NCP. The diversity of sizes and mixing states of BC-containing particles in different regions result in variations in observed AE values. In general, high AE values have been observed in polluted urban areas, such as Xian (1.8 at 870 nm) (Wang et al., 2014), Guangzhou (1.5 at 550 nm) (Wu et al., 2018) and Beijing (1.6 at 550 nm) (Zhao et al., 2020), and low values have been observed in relatively clean areas, such as Sacramento (1.06 at 532 nm) (Cappa et al., 2012) and Fontana (1.22 at 532 nm) (Cappa et al., 2019). Therefore, the results obtained with an AE of 1.5 for the whole area may underestimate the direct radiative effects of BC in the most heavily polluted areas and overestimate the effects of BC in clean areas in NCP. In the future, multi-model comparisons and evaluations of the aging processes of BC particles should be conducted in China.

Data availability

The WRF-Chem model is available at https://www2.mmm.ucar.edu/wrf/users/downloads.html (last access: 7 July 2020). The observations and simulation results are available upon request from the corresponding authors (hongliao@nuist.edu.cn; yang.yang@nuist.edu.cn).

CRediT authorship contribution statement

Donglin Chen: Conceptualization, Methodology, Software, Data curation, Visualization, Writing - original draft. **Hong Liao:** Writing - review & editing, Supervision, Conceptualization, Funding acquisition. **Yang Yang:** Conceptualization, Investigation, Formal analysis, Writing - review & editing. **Lei Chen:** Software, Validation, Supervision. **Hailong Wang:** Writing - review & editing, Validation, Supervision.

Declaration of competing interest

The authors declare that they have no known competing financial interests or personal relationships that could have appeared to influence the work reported in this paper.

Acknowledgements

This work was supported by the National Key Research and Development Program of China (grant no. 2019YFA0606804), the National Natural Science Foundation of China (grant no. 91744311), and the Major Research Plan of the National Social Science Foundation (grant no. 18ZDA052). H. Wang was supported by the U.S. Department of Energy (DOE), Office of Science, Office of Biological and Environmental Research (BER), Earth and Environmental System Modelling (EESM) program. The Pacific Northwest National Laboratory (PNNL) is operated for DOE by the Battelle Memorial Institute under contract DE-AC05-76RLO1830.

References

Barbaro, E., de Arellano, J.V.G., Ouwersloot, H.G., Schroter, J.S., Donovan, D.P., Krol, M.C., 2014. Aerosols in the convective boundary layer: shortwave radiation effects on the coupled land-atmosphere system. J. Geophys. Res.-Atmos. 119, 5845–5863. https://doi.org/10.1002/2013JD021237.

Barnard, J.C., Fast, J.D., Paredesmiranda, G., Arnott, W.P., Laskin, A., 2010. Technical note: evaluation of the WRF-Chem "aerosol chemical to aerosol optical properties" module using data from the MILAGRO campaign. Atmos. Chem. Phys. 10, 7325–7340. https://doi.org/10.5194/acp-10-7325-2010.

Bond, T.C., Doherty, S.J., Fahey, D.W., Forster, P.M., Berntsen, T., DeAngelo, B.J., Flanner, M.G., Ghan, S., Karcher, B., Koch, D., Kinne, S., Kondo, Y., Quinn, P.K., Sarofim, M.C., Schultz, M.G., Schulz, M., Venkataraman, C., Zhang, H., Zhang, S., Bellouin, N.,

Guttikunda, S.K., Hopke, P.K., Jacobson, M.Z., Kaiser, J.W., Klimont, Z., Lohmann, U., Schwarz, J.P., Shindell, D., Storlvmo, T., Warren, S.G., Zender, C.S., 2013. Bounding the role of black carbon in the climate system: a scientific assessment. J. Geophys. Res.-Atmos. 118, 5380–5552. https://doi.org/10.1002/jgrd.50171.

Bond, T.C., Habib, G., Bergstrom, R., 2016. Limitations in the enhancement of visible light absorption due to mixing state. J. Geophy. Res. 111. https://doi.org/10.1029/2006JD007315.

Cappa, C.D., Onasch, T.B., Massoli, P., Worsnop, D.R., Bates, T.S., Cross, E.S., Davidovits, P., Hakala, J., Hayden, K.L., Jobson, B.T., Kolesar, K.R., Lack, D.A., Lerner, B.M., Li, S.-M., Mellon, D., Nuaaman, I., Olfert, J.S., Petäjä, T., Quinn, P.K., Song, C., Subramanian, R., Williams, E.J., Zaveri, R.A., 2012. Radiative absorption enhancements due to the mixing state of atmospheric black carbon. Science 337, 1078–1081. https://doi.org/10.1126/science.1223447.

Cappa, C.D., Zhang, X., Russell, L.M., Collier, S., Lee, A.K.Y., Chen, C.-L., Betha, R., Chen, S., Liu, J., Price, D.J., Sanchez, K.J., McMeeking, G.R., Williams, L.R., Onasch, T.B., Worsnop, D.R., Abbatt, J., Zhang, Q., 2019. Light absorption by ambient black and brown carbon and its dependence on black carbon coating state for two California, USA cities in winter and summer. J. Geophys. Res. 124, 1550–1577. https://doi.org/10.1029/2018JD029501.

Chapman, E.G., Gustafson, W.I., Easter, R.C., Barnard, J.C., Ghan, S.J., Pekour, M.S., Fast, J.D., 2009. Coupling aerosol-cloud-radiative processes in the WRF-Chem model: investigating the radiative impact of elevated point sources. Atmos. Chem. Phys. 9, 945–964. https://doi.org/10.5194/acp-9-945-2009.

Chen, X., Wang, Z., Yu, F., Pan, X., Li, J., Ge, B., Wang, Z., Hu, M., Yang, W., Chen, H., 2017. Estimation of atmospheric aging time of black carbon particles in the polluted atmosphere over central-eastern China using microphysical process analysis in regional chemical transport model. Atmos. Environ. 163, 44–56. https://doi.org/10.1016/j.atmosenv.2017.05.016.

Chen, L., Zhu, J., Liao, H., Gao, Y., Qiu, Y., Zhang, M., Liu, Z., Li, N., Wang, Y., 2019. Assessing the formation and evolution mechanisms of severe haze pollution in the Beijing–Tianjin–Hebei region using process analysis. Atmos. Chem. Phys. 19, 10845–10864. https://doi.org/10.5194/acp-19-10845-2019.

Crutzen, P.J., 1973. A discussion of the chemistry of some minor constituents in the stratosphere and troposphere, Pure Appl. Geophys. 106, 1385–1399. https://doi.org/10.1007/BF00881092.

Cui, X., Wang, X., Yang, L., Chen, B., Chen, J., Andersson, A., Gustafsson, O., 2016. Radiative absorption enhancement from coatings on black carbon aerosols. Sci. Total Environ. 551, 51–56. https://doi.org/10.1016/j.scitotenv.2016.02.026.

Curci, G., Hogrefe, C., Bianconi, R., Im, U., Balzarini, A., Baro, R., Brunner, D., Forkel, R., Giordano, L., Hirtl, M., 2014. Uncertainties of simulated aerosol optical properties induced by assumptions on aerosol physical and chemical properties: An AQMEII-2 perspective. Atmos. Environ. 115, 541–552. https://doi.org/10.1016/j.atmosenv.2014.09.009.

Dickerson, R.R., Kondragunta, S., Stenchikov, G.L., Civerolo, K., Doddridge, B.G., Holben, B.N., 1997. The impact of aerosols on solar ultraviolet radiation and photochemical smog. Science 278, 827–830. https://doi.org/10.1126/science.278.5339.827.

Ding, A., Huang, X., Nie, W., Sun, J., Kerminen, V.M., Petaja, T., Su, H., Cheng, Y., Yang, X., Wang, M., 2016. Enhanced haze pollution by black carbon in megacities in China. Geophys. Res. Lett. 43, 2873–2879. https://doi.org/10.1002/2016GL067745.

Ding, S., Liu, D., Zhao, D., Hu, K., Tian, P., Zhou, W., Huang, M., Yang, Y., Wang, F., Sheng, J., 2019. Size-related physical properties of black carbon in the lower atmosphere over Beijing and Europe. Environ. Sci. Technol. 53, 11112–11121. https://doi.org/10.1021/acs.est.9b03722.

Ding, Q., Sun, J., Huang, X., Ding, A., Zou, J., Yang, X., Fu, C., 2019. Impacts of black carbon on the formation of advection-radiation fog during a haze pollution episode in eastern China. Atmos. Chem. Phys. 19, 7759–7774. https://doi.org/10.5194/acp-19-7759-2019.

Emmons, L.K., Walters, S., Hess, P.G., Lamarque, J., Pfister, G., Fillmore, D., Granier, C., Guenther, A., Kinnison, D.E., Laepple, T., 2010. Description and evaluation of the model for ozone and related chemical tracers, version 4 (MOZART-4). Geosci. Model Dev. 3, 43–67. https://doi.org/10.5194/gmd-3-43-2010.

Ferrero, L., Castelli, M., Ferrini, B., Moscatelli, M., Perrone, M., Sangiorgi, G., Dangelo, L., Rovelli, G., Moroni, B., Scardazza, F., 2014. Impact of black carbon aerosol over Italian basin valleys: high-resolution measurements along vertical profiles, radiative forcing and heating rate. Atmos. Chem. Phys. 14, 9641–9664. https://doi.org/10.5194/acp-14-9641-2014.

Flanner, M.G., Zender, C.S., Randerson, J.T., Rasch, P.J., 2007. Present-day climate forcing and response from black carbon in snow. J. Geophys. Res.-Atmos. 112. https://doi.org/10.1029/2006JD008003.

Forkel, R., Werhahn, J., Hansen, A.B., Mckeen, S.A., Peckham, S.E., Grell, G.A., Suppan, P., 2011. Effect of aerosol-radiation feedback on regional air quality – a case study with WRF/Chem. Atmos. Environ. 53, 202–211. https://doi.org/10.1016/j.atmosenv.2011.10.009.

Fuller, K.A., Malm, W.C., Kreidenweis, S.M., 1999. Effects of mixing on extinction by carbonaceous particles. J. Geophys. Res. 104, 15941–15954. https://doi.org/10.1029/1998JD100069.

Gao, Y., Zhang, M., Liu, Z., Wang, L., Wang, P., Xia, X., Tao, M., Zhu, L., 2015. Modeling the feedback between aerosol and meteorological variables in the atmospheric boundary layer during a severe fog–haze event over the North China Plain. Atmos. Chem. Phys. 15, 4279–4295. https://doi.org/10.5194/acp-15-4279-2015.

Gao, M., Carmichael, G.R., Wang, Y., Saide, P.E., Yu, M., Xin, J., Liu, Z., Wang, Z., 2016. Modeling study of the 2010 regional haze event in the North China Plain. Atmos. Chem. Phys. 16, 1673–1691. https://doi.org/10.5194/acp-16-1673-2016.

Gao, J., Zhu, B., Xiao, H., Kang, H., Hou, X., Yin, Y., Zhang, L., Miao, Q., 2017. Diurnal variations and source apportionment of ozone at the summit of Mount Huang, a rural site in Eastern China. Environ. Pollut. 222, 513–522. https://doi.org/10.1016/j.envpol.2016.11.031.

Gao, J., Zhu, B., Xiao, H., Kang, H., Pan, C., Wang, D., Wang, H., 2018. Effects of black carbon and boundary layer interaction on surface ozone in Nanjing, China. Atmos. Chem. Phys. 18, 7081–7094. https://doi.org/10.5194/acp-18-7081-2018.

Guenther, A., Karl, T., Harley, P., Wiedinmyer, C., Palmer, P.I., Geron, C., 2006. Estimates of global terrestrial isoprene emissions using MEGAN (model of emissions of gases and aerosols from nature). Atmos. Chem. Phys. 6, 3181–3210. https://doi.org/10.5194/acp-6-3181-2006.

Huang, X., Song, Y., Zhao, C., Cai, X., Zhang, H., Zhu, T., 2015. Direct radiative effect by multicomponent aerosol over China, J. Climate 28, 3472–3495. https://doi.org/10.1175/jcli-d-14-00365.1.

Huang, X., Wang, Z., Ding, A., 2018. Impact of aerosol-PBL interaction on haze pollution: multiyear observational evidences in North China. Geophys. Res. Lett. 45, 8596–8603. https://doi.org/10.1029/2018GL079239.

Jacobson, M.Z., 2001. Strong radiative heating due to the mixing state of black carbon in atmospheric aerosols. Nature 409, 695–697. https://doi.org/10.1038/350555181.

Ji, D., Li, L., Pang, B., Xue, P., Wang, L., Wu, Y., Zhang, H., Wang, Y., 2017. Characterization of black carbon in an urban-rural fringe area of Beijing. Environ. Pollut. 223, 524–534. https://doi.org/10.1016/j.envpol.2017.01.055.

Ji, D., Yan, Y., Wang, Z., He, J., Liu, B.X., Sun, Y., Gao, M., Li, Y., Cao, W., Cui, Y., 2018. Two-year continuous measurements of carbonaceous aerosols in urban Beijing, China: temporal variations, characteristics and source analyses. Chemosphere 200, 191–200. https://doi.org/10.1016/j.chemosphere.2018.02.067.

Laborde, M., Crippa, M., Tritscher, T., Juranyi, Z., Decarlo, P.F., Temimeroussel, B., Marchand, N., Eckhardt, S., Stohl, A., Baltensperger, U., 2013. Black carbon physical properties and mixing state in the European megacity Paris. Atmos. Chem. Phys. 13, 5831–5856. https://doi.org/10.5194/acp-13-5831-2013.

Li, K., Liao, H., Zhu, J., Moch, J.M., 2016. Implications of RCP emissions on future $PM_{2.5}$ air quality and direct radiative forcing over China. J. Geophys. Res.-Atmos. 121. https://doi.org/10.1002/2016JD025623.

Li, M., Zhang, Q., Kurokawa, J., Woo, J., He, K.B., Lu, Z., Ohara, T., Song, Y., Streets, D.G., Carmichael, G.R., Cheng, Y., Hong, C., Huo, H., Jiang, X., Kang, S., Liu, F., Su, H., Zheng, B., 2017. MIX: a mosaic Asian anthropogenic emission inventory under the international collaboration framework of the MICS-Asia and the HTAP. Atmos. Chem. Phys. 17, 935–963. https://doi.org/10.5194/acp-17-935-2017.

Liu, X., Zhang, Y., Jung, J., Gu, J., Li, Y., Guo, S., Chang, S., Yue, D., Lin, P., Kim, Y.J., 2008. Research on the hygroscopic properties of aerosols by measurement and modeling during CAREBeijing-2006. J. Geophys. Res. 114. https://doi.org/10.1029/2008JD010805.

Liu, D., Allan, J.D., Young, D.E., Coe, H., Beddows, D.C.S., Fleming, Z.L., Flynn, M., Gallagher, M.W., Harrison, R.M., Lee, J.D., 2014. Size distribution, mixing state and source apportionment of black carbon aerosol in London during wintertime. Atmos. Chem. Phys. 14, 10061–10084. https://doi.org/10.5194/acp-14-10061-2014.

Liu, X., Ma, P.L., Wang, H., Tilmes, S., Singh, B., Easter, R.C., Ghan, S.J., Rasch, P.J., 2016. Description and evaluation of a new four-mode version of the modal aerosol module (MAM4) within version 5.3 of the Community Atmosphere Model. Geosci. Model Dev. 9 (2), 505–522. https://doi.org/10.5194/gmd-9-505-2016.

Liu, D., Whitehead, J.D., Alfarra, M.R., Reyesvillegas, E., Spracklen, D.V., Reddington, C.L., Kong, S., Williams, P.I., Ting, Y., Haslett, S., 2017. Black-carbon absorption enhancement in the atmosphere determined by particle mixing state. Nat. Geosci. 10, 184–188. https://10.1038/ngeo2901.

Liu, D., Joshi, R., Wang, J., Yu, C., Allan, J.D., Coe, H., Flynn, M., Xie, C., Lee, J.D., Squires, F., 2019. Contrasting physical properties of black carbon in urban Beijing between winter and summer. Atmos. Chem. Phys. 19, 6749–6769. https://doi.org/10.5194/acp-19-6749-2019.

Lohmann, U., Feichter, J., Penner, J.E., Leaitch, R., 1999. Indirect effect of sulfate and carbonaceous aerosols: a mechanistic treatment. J. Geophys. Res. 105, 12193–12206. https://doi.org/10.1029/1999JD901199.

Lou, S., Yang, Y., Wang, H., Smith, S.J., Qian, Y., Rasch, P.J., 2019. Black carbon amplifies haze over the North China plain by weakening the East Asian winter monsoon. Geophys. Res. Lett. 46, 452–460. https://doi.org/10.1029/2018GL080941.

Matsui, H., 2016a. Black carbon simulations using a size- and mixing-state-resolved three-dimensional model: 1. Radiative effects and their uncertainties. J. Geophys. Res.-Atmos. 121, 1793–1807. https://doi.org/10.1002/2015JD023998.

Matsui, H., 2016b. Black carbon simulations using a size- and mixing-state-resolved three-dimensional model: 2. Aging timescale and its impact over East Asia. J. Geophys. Res.-Atmos. 121, 1808–1821. https://doi.org/10.1002/2015JD023999.

Matsui, H., Hamilton, D.S., Mahowald, N.M., 2018. Black carbon radiative effects highly sensitive to emitted particle size when resolving mixing-state diversity. Nat. Commun. 9, 3446. https://doi.org/10.1038/s41467-018-05635-1.

Moteki, N., Kondo, Y., Miyazaki, Y., Takegawa, N., Komazaki, Y., Kurata, G., Shirai, T., Blake, D.R., Miyakawa, T., Koike, M., 2007. Evolution of mixing state of black carbon particles: aircraft measurements over the western Pacific in March 2004. Geophys. Res. Lett. 34. https://doi.org/10.1029/2006GL028943.

Peng, J., Hu, M., Guo, S., Du, Z., Zheng, J., Shang, D., Zamora, M.L., Zeng, L., Shao, M., Wu, Y., 2016. Markedly enhanced absorption and direct radiative forcing of black carbon under polluted urban environments. Proc. Natl. Acad. Sci. USA 113, 4266–4271. https://doi.org/10.1073/pnas.1602310113.

Qiu, Y., Hong, L., Zhang, R., Hu, J., 2017. Simulated impacts of direct radiative effects of scattering and absorbing aerosols on surface layer aerosol concentrations in China during a heavily polluted event in February 2014. J. Geophys. Res.-Atmos., 122 https://doi.org/10.1002/2016JD026309.

Samset, B.H., Myhre, G., 2011. Vertical dependence of black carbon, sulphate and biomass burning aerosol radiative forcing. Geophys. Res. Lett. 38. https://doi.org/10.1029/2011GL049697.

Samset, B.H., Myhre, G., Herber, A., Kondo, Y., Zhang, K., 2014. Modelled black carbon radiative forcing and atmospheric lifetime in AeroCom Phase II constrained by aircraft observation. Atmos. Chem. Phys. 14, 12456–12477. https://doi.org/10.5194/acp-14-12465-2014.

Schnaiter, M., Linke, C., Mohler, O., Naumann, K.H., Saathoff, H., Wagner, R., Schurath, U., Wehner, B., 2005. Absorption amplification of black carbon internally mixed with secondary organic aerosol. J. Geophys. Res. 110. https://10.1029/2005JD006046.

Schuster, G.L., Dubovik, O., Holben, B.N., 2006. Angstrom exponent and bimodal aerosol size distributions. J. Geophys. Res.-Atmos. 111. https://doi.org/10.1029/2005JD006328.

Stelson, A.W., 1990. Urban aerosol refractive index prediction by partial molar refraction approach. Environ. Sci. Technol. 24, 1676–1679. https://doi.org/10.1021/es00081a008.

Sun, Y., Zhuang, G., Tang, A., Wang, Y., An, Z., 2006. Chemical characteristics of $PM_{2.5}$ and PM_{10} in haze−fog episodes in Beijing. Environ. Sci. Technol. 40, 3148–3155. https://doi.org/10.1021/es051533g.

Sun, J.Y., Wu, C., Wu, D., Cheng, C., Li, M., Li, L., Deng, T., Yu, J.Z., Li, Y., Zhou, Q., 2020. Amplification of black carbon light absorption induced by atmospheric aging: temporal variation at seasonal and diel scales in urban Guangzhou. Atmos. Chem. Phys. 20, 2445–2470. https://10.5194/acp-20-2445-2020.

Takahama, S., Russell, L.M., Shores, C.A., Marr, L.C., Zheng, J., Levy, M., Zhang, R., Castillo, E., Rodriguezventura, J.G., Quintana, P.J.E., 2014. Diesel vehicle and urban burning contributions to black carbon concentrations and size distributions in Tijuana, Mexico, during the Cal-Mex 2010 campaign. Atmos. Environ. 88, 341–352. https://doi.org/10.1016/j.atmosenv.2013.09.057.

Tang, G., Zhu, X., Xin, J., Hu, B., Song, T., Sun, Y., Zhang, J., Wang, L., Cheng, M., Chao, N., Kong, L., Li, X., Wang, Y., 2017. Modelling study of boundary-layer ozone over northern China-part I: ozone budget in summer. Atmos. Res. 187, 128–137. https://doi.org/10.1016/j.atmosres.2016.10.017.

Wang, Q., Cao, J., Han, Y., Wang, G., Li, G., Wang, Y., Dai, W., Zhang, R., Zhou, Y., Psi, V., 2014. Mixing state of black carbon aerosol in a heavily polluted urban area of China: implications for light absorption enhancement, Aerosol Sci. Tech. 48, 689–697. https://doi.org/10.1080/02786826.2014.917758.

Wang, Q.Q., Jacob, D.J., Spackman, J.R., Perring, A.E., Schwarz, J.P., Moteki, N., Marais, E.A., Ge, C., Wang, J., Barrett, S.R.H., 2014. Global budget and radiative forcing of black carbon aerosol: constraints from pole-to-pole (HIPPO) observations across the Pacific. J. Geophys. Res. 119, 195–206. https://doi.org/10.1002/2013JD020824.

Wang, H., Xue, M., Zhang, X.Y., Liu, H.L., Zhou, C.H., Tan, S.C., Che, H.Z., Chen, B., Li, T., 2015. Mesoscale modeling study of the interactions between aerosols and PBL meteorology during a haze episode in Jing–Jin–Ji (China) and its nearby surrounding region – part 1: aerosol distributions and meteorological features. Atmos. Chem. Phys. 15, 3257–3275. https://doi.org/10.5194/acp-15-3257-2015.

Wang, J., Zhao, B., Wang, S., Yang, F., Xing, J., Morawska, L., Ding, A., Kulmala, M., Kerminen, V., Kujansuu, J., 2017. Particulate matter pollution over China and the effects of control policies. Sci. Total Environ. 584, 426–447. https://doi.org/10.1016/j.scitotenv.2017.01.027.

Wang, Z., Huang, X., Ding, A., 2018. Dome effect of black carbon and its key influencing factors: a one-dimensional modelling study. Atmos. Chem. Phys. 1-29. https://doi.org/10.5194/acp-18-2821-2018.

Watson-Parris, D., Schutgens, N., Reddington, C.L., Pringle, K.J., Liu, D., Allan, J.D., Coe, H., Carslaw, K.S., Stier, P., 2019. In situ constraints on the vertical distribution of global aerosol. Atmos. Chem. Phys. 19, 11765–11790. https://doi.org/10.5194/acp-19-11765-2019.

Wiedinmyer, C., Akagi, S.K., Yokelson, R.J., Emmons, L.K., Alsaadi, J.A., Orlando, J.J., Soja, A.J., 2011. The fire INventory from NCAR (FINN): a high resolution global model to estimate the emissions from open burning. Geosci. Model Dev. 4, 625–641. https://doi.org/10.5194/gmd-4-625-2011.

Wu, Y., Zhang, R., Tian, P., Tao, J., Hsu, S., Yan, P., Wang, Q., Cao, J., Zhang, X., Xia, X., 2016. Effect of ambient humidity on the light absorption amplification of black carbon in Beijing during January 2013. Atmos. Environ. 124, 217–223. https://doi.org/10.1016/j.atmosenv.2015.04.041.

Wu, C., Wu, D., Yu, J.Z., 2018. Quantifying black carbon light absorption enhancement with a novel statistical approach. Atmos. Chem. Phys. 18, 289–309. https://10.5194/acp-18-289-2018.

Xie, C., Xu, W., Wang, J., Liu, D., Ge, X., Zhang, Q., Wang, Q., Du, W., Zhao, J., Zhou, W., 2019. Light absorption enhancement of black carbon in urban Beijing in summer. Atmos. Environ. 213, 499–504. https://doi.org/10.1016/j.atmosenv.2019.06.041.

Xing, J., Wang, J., Mathur, R., Wang, S., Sarwar, G., Pleim, J.E., Hogrefe, C., Zhang, Y., Jiang, J., Wong, D.C., 2017. Impacts of aerosol direct effects on tropospheric ozone through changes in atmospheric dynamics and photolysis rates. Atmos. Chem. Phys. 17, 9869–9883. https://doi.org/10.5194/acp-17-9869-2017.

Yang, Y., Liao, H., Lou, S., 2016. Increase in winter haze over eastern China in recent decades: roles of variations in meteorological parameters and anthropogenic emissions. J. Geophys. Res. 121. https://doi.org/10.1002/2016JD025136.

Yang, Y., Wang, H., Smith, S.J., Ma, P., Rasch, P.J., 2017. Source attribution of black carbon and its direct radiative forcing in China. Atmos. Chem. Phys. 17, 4319–4336. https://doi.org/10.5194/acp-17-4319-2017.

Yang, Y., Smith, S.J., Wang, H., Mills, C.M., Rasch, P.J., 2019. Variability, timescales, and nonlinearity in climate responses to black carbon emissions. Atmos. Chem. Phys. 19, 2405–2420. https://doi.org/10.5194/acp-19-2405-2019.

Zhang, J., Rao, S.T., 1999. The role of vertical mixing in the temporal evolution of ground-level ozone concentrations. J. Appl. Meteorol. 38, 1674–1691. https://doi.org/10.1175/1520-0450(1999)038<1674:TROVMI>2.0.CO;2.

Zhang, R., Wang, G., Guo, S., Zamora, M.L., Ying, Q., Lin, Y., Wang, W., Hu, M., Wang, Y., 2015. Formation of urban fine particulate matter. Chem. Rev. 115, 3803–3855. https://doi.org/10.1021/acs.chemrev.5b00067.

Zhang, H., Guo, H., Hu, J., Ying, Q., Kleeman, M.J., 2019. Modeling atmospheric age distribution of elemental carbon using a regional age-resolved particle representation framework. Environ. Sci. Technol. 53, 270–278. https://doi.org/10.1021/acs.est.8b05895.

Zhao, D., Huang, M., Tian, P., He, H., Ding, D., 2019. Vertical characteristics of black carbon physical properties over Beijing region in warm and cold seasons. Atmos. Environ. https://doi.org/10.1016/j.atmosenv.2019.06.007.

Zhao, D., Liu, D., Yu, C., Tian, P., Hu, D., Zhou, W., Ding, S., Hu, K., Sun, Z., Huang, M., 2020. Vertical evolution of black carbon characteristics and heating rate during a haze event in Beijing winter. Sci. Total Environ. 709, 136251. https://doi.org/10.1016/j.scitotenv.2019.136251.